Synthesis and characterization of wide bandgap semiconductors doped with terbium for electroluminescent devices

Student:

Liz Margarita Montañez Huamán

Supervisor:

Dr. Roland Weingärtner

Dr. Harald Hoppe

Lima, February 2016

Abstract

In this work, stoichiometric, structural and light emission properties of amorphous wide bandgap semiconductor materials doped with terbium are presented. The amorphous nature of the thin films was confirmed by X-ray diffraction under grazing incidence. Fourier transform infrared spectroscopy spectra exhibit the formation of oxygen bonded elements and X-ray photoelectron spectroscopy reveals the formation of aluminum oxynitride and silicon oxycarbide as host matrices. The thin films were annealed at temperatures ranging from 300 °C to 1000 °C using a rapid thermal processing furnace. The highest light emission intensity for the case of aluminum oxynitride was obtained for terbium concentrations higher than 1 at% and for the annealing temperature at around 400 °C. Additionally, using the characterized films as active layer first electroluminescence devices were designed and investigated.

Resumen

En el presente trabajo de investigación se ha estudiado propiedades estequiometrias, estructurales y de emisión de luz de semiconductor de amplio ancho de banda dopados con terbio. La difracción de rayos-X en ángulo rasante confirma el estado amorfo de las películas. Los espectros de absorción infrarroja muestran la formación de óxidos en las películas y la espectroscopia de foto-electrones de rayos-X revela la formación de oxinitruro de aluminio y oxicarburo de silicio. Las películas han sido calentadas a temperaturas en el rango de 300 °C a 1000 °C en un horno de rápido procesamiento térmico. De acuerdo con el análisis de las medidas de fotoluminiscencia, la intensidad más alta de emisión de luz del terbio es para películas que tengan concentraciones de terbio mayores al 1at% y a una temperatura de tratamiento térmico de alrededor de 400 °C. Adicionalmente, las películas analizadas han sido usado como capas activas para el diseño de dispositivos electroluminiscentes.

Kurzfassung

In dieser Arbeit wurden die stöchiometrischen, strukturellen und Licht emittierenden Eigenschaften von amorphen Halbleitermaterialien mit großer Bandlücke und dotiert mit Terbium untersucht. Die amorphe Natur der dünnen Schichten wurde durch Röntgenbeugung unter niedrigen Einfallswinkel bestätigt. Die Fourier-Transformations-Infrarot Spektroskopie zeigt die Formation von Elementen mit Sauerstoffbindungen und die Röntgen-Photoelektronen-Spektroskopie deckt die Formation von Aluminium-Oxinitriden und Silizium-Oxicarbiden als Hostmatrix auf. Die dünnen Filme wurden in einem Rapid Thermal Processing Ofen bei Temperaturen im Bereich zwischen 300°C und 1000°C getempert. Die höchste Lichtemissionsintensität im Fall von Aluminium Sauerstoffnitrid wurde bei einer Terbiumkonzentration von höher als 1 at% und für Tempertemperaturen von ca. 400°C erreicht. Des Weiteren wurden mit den characterisierten Filmen als Aktivmaterial erste Bauelemente für Elektrolumineszenz entwickelt und untersucht.

I dedicate this thesis to my parents Basilio Montañez and Rufina Huamán and to my brother Kevin and sisters Geraldine, Nancy and Edith.

Contents

1. Introduction

Crystalline aluminum nitride (AlN) is a semiconductor with excellent properties like its wide bandgap of 6.2 eV, high chemical stability, high thermal conductivity and high dielectric breakdown voltage [1]. Owing to these properties, AlN can be used for opto-electronic devices which operate at high temperature, high voltage and high power [2]. Due to the wide bandgap of AlN, it is a suited epilayer template to produce deep ultraviolet (UV) light emitting diodes (LEDs) based on GaN with high crystalline quality, surface morphology, photoluminescence intensity, and good conductivity [3]. AlN has good transparency and high refractive index, therefore, it is widely used for anti-reflective coatings in solar cells [4]. Recent studies have demonstrated its potential application as passivation emitter rear cell (PERC) as it is showing a low interface defect density and high density of negative charges [5]. Silicon carbide (SiC) is another wide bandgap semiconductor which has been the subject of several investigations due to its outstanding optical, electrical and mechanical properties [6–8]. These excellent properties allow SiC to be an optimal material for several potential applications in optoelectronic and photo-electrochemical devices [9].

Amorphous AlN and SiC have the advantage to be produced rather simply and inexpensively without the drawback of losing dramatically the aforementioned features [10]. On the other hand, it is possible to perform bandgap engineering of both amorphous layers using successive thermal annealing treatments [10]. Nowadays, SiC based materials, like amorphous silicon carbon nitride (*a*-SiCN) and silicon oxycarbonitride (*a*-SiCNO) are very promising materials for optoelectronic devices because of e.g. their tunable wide bandgap. Additionally, their high mechanical strength and thermal conductivity are well suited for microelectromechanical systems (MEMS) [6,7]. The addition of nitrogen into the SiC matrix produces two effects: on the one hand, it enhances the electrical conductivity, whereas on the other hand it produces a decrease in the optical bandgap [8]. Amorphous AlN has proven to be an ideal host for rare earths (RE) ions and thus opening the possibility for further applications in electroluminescent panels [11].

RE doped wide bandgap semiconductors have been the subject of several investigations for various optoelectronic applications [12]. Their main feature is that their emission spectra hardly depend on the host matrix. This feature is due to the fact that the electronic transitions involved occur between the f-shell energy levels that are shielded from the bonding electrons. Additionally, the RE light emission covers the basic colors in the visible region: blue (Tm^{3+}), green (Tb^{3+}) and red (Eu^{3+}) and the emission intensity can be enhanced by subsequent thermal annealing treatments and bandgap engineering of the host matrix [13,14]. Notwithstanding, the drawback of the RE emission application in optoelectronic devices is the concentration and temperature quenching effect, which limits the intensity of light emission [13]. On the other hand, the role that the electronic defects play in the excitation mechanism is still an open field for research [15]. Wide bandgap semiconductors doped with REs have been extensity used as active

layers in electroluminescence (EL) devices [11,16,17]. Nowadays, they are attractive in passivation of solar cells due their up-conversion and down-conversion properties[18].

The present thesis was developed in the framework of a double master degree program in Material Science and Engineering between the Pontificia Universidad Católica del Perú (PUCP) and the Technische Universität Ilmenau (TU-Ilmenau). The scientific group of Material Science, section Physics at PUCP investigates amorphous wide bandgap semiconductor materials doped with rare earths. Purposes are the production of thin films and their optical and luminescence characterization in order to investigate the ability of these materials for opto-electronic and EL devices. Next steps are the study of the stoichiometry and structural properties of these layers and also their direct implementation as active materials in EL devices. Therefore, the first aim of this thesis is the study of the stoichiometric, structural, and luminescence properties of the amorphous undoped and terbium doped AlN and SiC layers. The second aim is the design and production of EL devices using terbium doped AlN and SiC as active layers. The production of the active layers was done in the Material Science laboratory at PUCP. The analytic characterizations were performed in the Institut für Mikro-und Nanotechnologie (IMN) of the TU-Ilmenau.

The present thesis is divided into six sections: introduction, state of the art, analytic techniques, design of the EL devices, result and discussions, and conclusions. The state of the art comprises the fundamental properties and the luminescence mechanisms of the RE ions as well as the structure and working principles of the EL devices. In section 3, the analytic techniques will be described. The characterization of the layers was done by the following analytic techniques: Fourier transform infrared spectroscopy (FTIR), X-ray emission spectroscopy (XPS), X-ray diffraction (XRD), cathodoluminescence (CL) and electroluminescence (EL) measurements.

In section 4, the design of the EL devices will be explained. Two kinds of EL devices were designed: alternating current thin film electroluminescence (ACTFEL) devices and direct current thin film electroluminescence (DCTFEL) devices. For both types of devices conventional and inverted structure were designed. Results will be discussed in section 5 and finally the conclusions will be presented in section 6.

2. State of the art

In the following section, the state of the art will be addressed briefly. First, physical properties of wide bandgap (WBG) semiconductors are explained with emphasis on aluminum nitride and silicon carbide. They will be compared to the traditional silicon. Furthermore, fundamental characteristics of rare earths will be described with a focus on the trivalent terbium (Tb^{+3}). The luminescent mechanisms of REs ions and also energy transfer processes will be addressed. Finally, the working principles of EL devices will be presented. Two kinds of devices will be treated. In the case of the ACTFEL devices, the active film is sandwiched by insulating layers to prevent breakdown. Hole transport layer (HTL) and electron transport layer (ETL) are incorporated in the DCTFEL devices in order to improve the injection of the holes and electrons.

2.1 Wide bandgap semiconductors

Semiconductors with bandgap energies larger than 2 eV are defined as wide bandgap semiconductors materials. Those materials are employed in wide range of opto-electronic and electroluminescent devices e.g. light emitting diodes (LEDs) operating in the blue and ultraviolet spectral range [19]. WBG semiconductors can be classified in several groups: group III nitrides, group II oxides, group II chalcogenides, group IV-IV compounds and diamond. Figure 2.1 shows the bandgap versus the lattice constant of the principal WBG semiconductors. The black and white circles represent the direct and indirect bandgap, respectively.

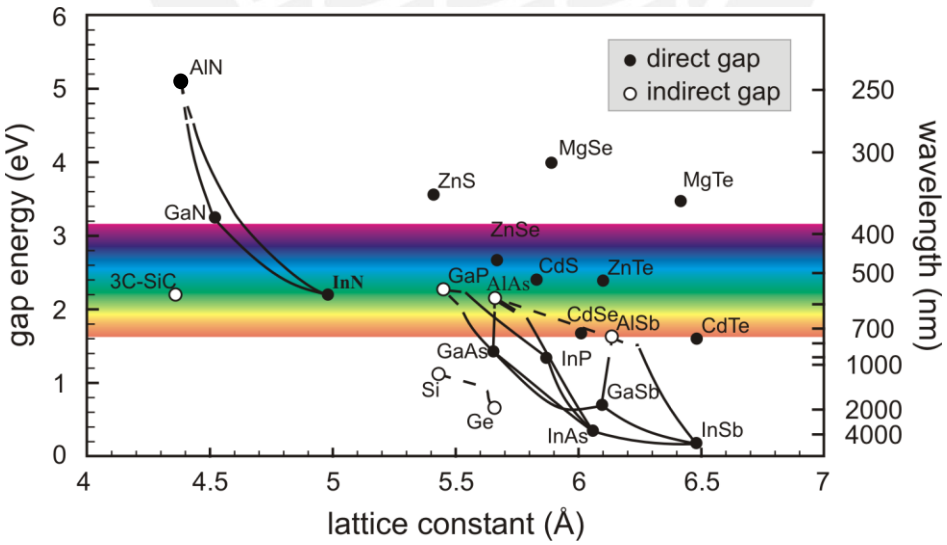

Figure 2.1 Relationship between the bandgap energy and lattice constant of the main direct and indirect wide bandgap semiconductors. The right-hand scale shows the emission wavelength [20]. The values of further important semiconductors such as Si and Ge are included.

Table 2.1 shows the main physical properties of WBG semiconductors as well as the values of the silicon for comparison reasons.

Table 2.1 Physical properties of WBG semiconductors at 300 K. Some properties of the diamond are at room temperature (RT). The values for the silicon are also included for comparison reasons [1,19,21]**.**

	Si	**AlN (W)**	**SiC (4H)**	**ZnO**	**Diamond**
Energy gap (eV)	1.12	6.2	3.26	3.4	5.5 (RT)
Transition	indirect	direct	indirect	direct	indirect
Refractive index	2.4	2.2	2.55	2.03	3.5
Thermal conductivity ($Wcm^{-1}K^{-1}$)	1.56	2.9	3.0-3.8	0.6	20.9
Electron mobility ($cm^2V^{-1}s^{-1}$)	1450	300	948	125	2000 (RT)
Hole mobility ($cm^2V^{-1}s^{-1}$)	370	14	98.5	165	2100 (RT)
Electrical conductivity ($\Omega^{-1}cm^{-1}$)	-	10^{-11}-10^{-13}	-	1-50	-
Breakdown field ($MVcm^{-1}$)	0.3	1.2	3.0	-	4.0
Melting point (K)	1687	3025	2073	2242	4100

Silicon carbide is a binary WBG semiconductor, which has several different polytypes, Fisher *et al.* mentioned more than 250 polytypes [22]. The most important are: 6H-SiC, 4H-SIC and 3C-SiC. All polytypes consist of silicon atoms bounded with four carbons atoms in a tetrahedral arrangement [23]. SiC has three crystal systems: cubic, hexagonal and rhombohedral. Every structure has a defined staking sequence of the tetrahedral Si and C atoms [24]. The advantage of SiC over the other WBG semiconductors is its robust mechanical property. The Vickers hardness of SiC reported by Yonenaga is 25 GPa [25]. The disadvantage of SiC is its indirect optical bandgap, despite that, it can be used as optical device, as LEDs in the blue and ultraviolet region [26]. SiC is also attractive for diodes (Schottky diode), transistor, MEMS, ultraviolet photodiodes and LEDs.

AlN has a wurtzite or zincblende structure with hexagonal and cubic unit cell, respectively. The wurtzite structure is composed of two interpenetrating hexagonal close packed (hcp) sublattices and exhibits a direct bandgap, whereas the zincblende structure is composed of two interpenetrating face centered cubic (fcc) sublattices with indirect bandgap [21]. Due the large bandgap of 6.2 eV of the AlN, it is a good candidate for the production of LEDs emitting in the deep UV region[19]. As it is exhibiting a high breakdown field AlN is used as insulating material and as passivation of boron emitters [5].

WBG semiconductors present better properties than the conventional Si. Due their wide bandgap, they are transparent in the visible region (SiC) and also in the UV (AlN). WBG

semiconductors present high melting points and also their breakdown is four times (SiC), ten times (AlN) or up to thirteen times (diamond) higher than Si. However, with the exception of diamond, WBG cannot reach the high electron and hole mobility like Si.

2.2 Rare earth elements

2.2.1 Physical properties of RE elements

Rare earths, also known as lanthanides, comprises 15 elements with atomic number ranging from 57 (Lanthanum) to 71 (Lutetium). REs are abundant in nature. They can be found mixed with other minerals. Nevertheless, their name is attributed to the difficulty of separating them from the minerals. The emission of REs covers the basic color of the visible light, emitting in the red, green and blue regions with Europium, Terbium and Thulium, respectively. All REs + ions have the closed noble gas Xenon ([Xe]=$1s^2 2s^2 2p^6 3s^2 3p^6 3d^{10} 4s^2 4p^6 4d^{10} 5s^2 5p^6$) configurations and only differ in the number of electrons in the f-shell. Figure 2.2 depicts the radial distribution of the 4f, 5s, 5p, 5d, 6s and 6d orbits of the samarium. The 4f electron is shielded by the 5s and 5p shells, therefore, it is call an internal electron shell. 5p is an external electron shell regarding the 4f and internal regarding 6s.

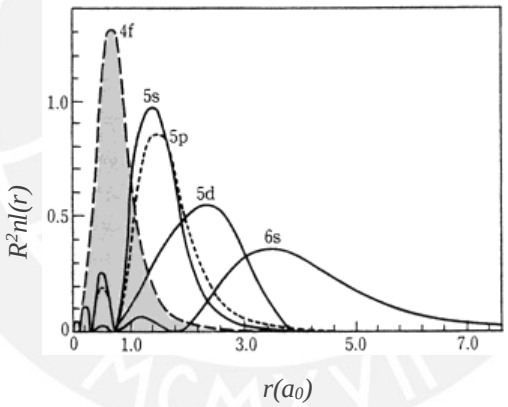

Figure 2.2 Radial distribution function of the electronic densities of the samarium [27].

The fundamental properties of the 15 lanthanides are shown in Table 2.2. The main feature of the REs regarding its luminescent properties is that the electrons in the partially filled 4f shells are shielded by the electrons in the closed 5s and 5p shells, thus, the energy levels of the 4f are weekly affected by the ligand ions of the host matrix. Therefore, the emission spectra of the RE exhibit sharp and well defined peaks. Due to their well-defined emission spectra they are good candidates as luminescent centers for the fabrication of EL devices. REs are usually dopants in wide bandgap semiconductors matrices as trivalent or divalent ions. Only three divalent lanthanides are stable in nature such as Samarium, Europium and Ytterbium [28].

Table 2.2 Electronic configuration of the REs elements, ionic radius for trivalent REs with coordination number 8 and atomic radius [29].

Z	*Element*	*Electronic configuration of neutral atoms*					*Electronic configuration of trivalent ions*	*Ionic radius of trivalent ions (pm)*	*Atomic radius (pm)*
		4f	*5s*	*5p*	*5d*	*6s*			
57	La	0	2	6	1	2	$[Xe]4f^{0}$	116.0	186
58	Ce	1	2	6	1	2	$[Xe]4f^{1}$	114.3	182.5
59	Pr	3	2	6		2	$[Xe]4f^{2}$	112.6	182.8
60	Nd	4	2	6		2	$[Xe]4f^{3}$	110.9	182.1
61	Pm	5	2	6		2	$[Xe]4f^{4}$	-	181.0
62	Sm	6	2	6		2	$[Xe]4f^{5}$	107.9	180.4
63	Eu	7	2	6		2	$[Xe]4f^{6}$	106.6	204.2
64	Gd	7	2	6	1	2	$[Xe]4f^{7}$	105.3	180.4
65	Tb	9	2	6		2	$[Xe]4f^{8}$	104.4	178.3
66	Dy	10	2	6		2	$[Xe]4f^{9}$	102.7	177.4
67	Ho	11	2	6		2	$[Xe]4f^{10}$	101.5	176.6
68	Er	12	2	6		2	$[Xe]4f^{11}$	100.4	175.7
69	Tm	13	2	6		2	$[Xe]4f^{12}$	99.4	174.6
70	Yb	14	2	6		2	$[Xe]4f^{13}$	98.5	193.9
71	Lu	14	2	6	1	2	$[Xe]4f^{14}$	97.7	173.5

The atomic number of the REs increases gradually by one from La to Lu. The added electron fills the incomplete 4f shell instead of the outer shells. Since the screening constant of the 4f electrons in trivalent ions is less than one (around 0.85 [29]), the attraction between the nucleus and the outer electron increases, producing a shrinkage of the electron cloud and, therefore, a gradual decrease in the size of the trivalent ions. This phenomenon is called, lanthanide contraction and influences the properties of the REs elements. Due to the lanthanide contraction, the atomic radio also decreases with the increase of the atomic number, except in the case of Europium and Ytterbium. However, since the shielding effect of the inner 4f shells on atoms is not as strong as in ions, the lanthanide contraction is weaker in the atoms than in the ions.

2.2.2 Electronic configuration of the trivalent terbium (Tb^{3+})

Terbium (Tb^{3+}) is a trivalent RE ion with an atomic number of 65 and an electronic configuration of [Xe] $4f^{8}$. Tb^{3+} presents sharp spectral lines in the green region because of the $^{5}D_{4}\rightarrow{}^{7}F_{j}$ transitions. It also can emit weekly in the blue spectral region due to the $^{5}D_{3}\rightarrow{}^{7}F_{j}$ transitions.

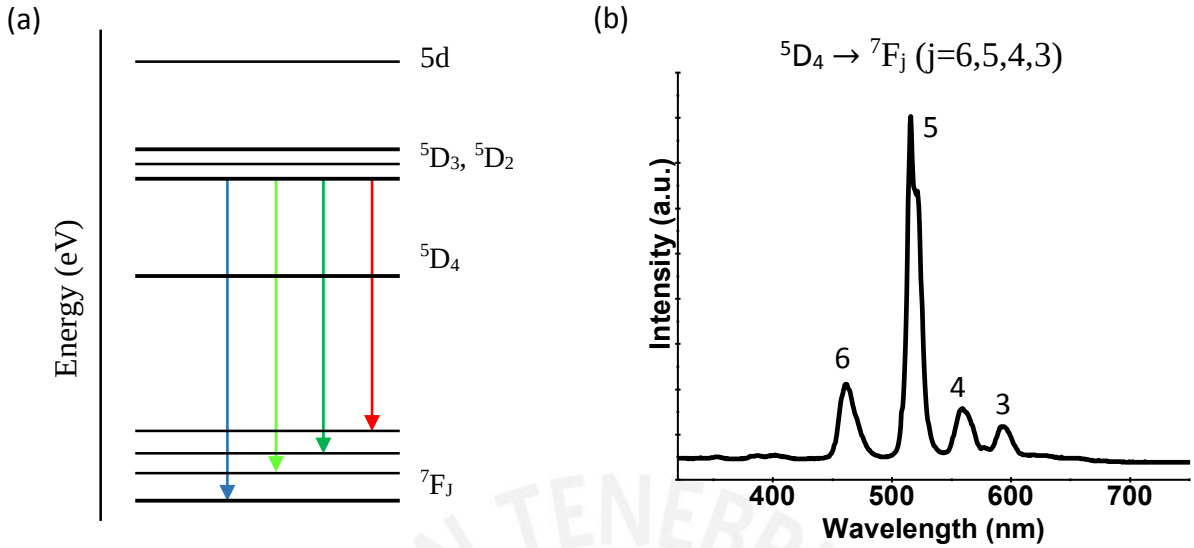

Figure 2.3 Electronic transitions [30] (a) and CL emission spectra (b) of Tb^{+3}.

Figure 2.3(a) shows the electronic transition of the Tb^{3+}. The $^5D_4 \rightarrow {}^7F_j$ transitions allow luminescence in four wavelengths: 489; 543; 586 and 621 nm. Figure 2.3 (b) shows a CL spectrum of Tb^{3+}, where only the $^5D_4 \rightarrow {}^7F_j$ transitions are observed. Further detail concerning this spectrum will be presented in section 5 (results and conclusions).

2.3 Emission mechanism of luminescent materials: excitation process and energy transfer.

a) Excitation process

Luminescent materials emit light when they absorb energy. In the case of wide bandgap materials doped with REs, the absorption process takes place in the REs ions as well as in the host matrix. The luminescence of the host matrix is usually broad and with low intensity depending on the temperature during the measurement or the excitation source [31]. In contrast to that, the luminescence of the REs shows very strong narrow lines (see Figure 2.3 b). The emission of light from luminescent materials can be measured by different techniques: PL, CL and EL. PL uses photons to excite the active material while CL uses electrons. EL uses DC or AC current. The excitation process can involve recombination of electron-hole pairs, energy transfer or impact ionization.

b) Carrier recombination mechanism

Recombination mechanism can be intrinsic or extrinsic. Intrinsic recombination occurs directly band to band and can be divided in radiative recombination and Auger recombination. In the radiative band-band recombination, electron-hole pairs annihilate each other and the excess energy is released as a photon. Auger band-band recombination involves the interaction of three particles, where the excess energy released by the recombination of the electron-hole pair is transferred to a third particle and is afterward released as phonons to the crystal (thermalization)

[32]. Extrinsic recombination in contrast to the extrinsic case occurs via discrete energy levels (defect level) within the bandgap. This process is known as Shockley Read Hall (SRH) recombination. The discrete level can act as a recombination center, where electrons and holes can be captured by the defect level and annihilate each other. When the defect level, successively emits an electron in the conduction band and a hole in the valence band, the discrete level acts as a generation center. In the case of the carrier captured by the defect level and afterwards injected back into the band from which it came, the discrete level acts as trap center [32].

c) Energy transfer

Consider two ions D (donor) and A (acceptor), separated by a distance R. The ion D is considered to transfer its energy from an excited state to the ion A in the ground state. When the energy between the ground and excited state of both ions is the same, the transfer is called resonant. Energy transfer can occur in two principal forms: resonant radiative energy transfer and resonant non-radiative energy transfer. When the ions are not in resonance, multi-phonons assist the energy transfer. In the case of equal ions, cross-relaxation can happen (see Figure 2.4).

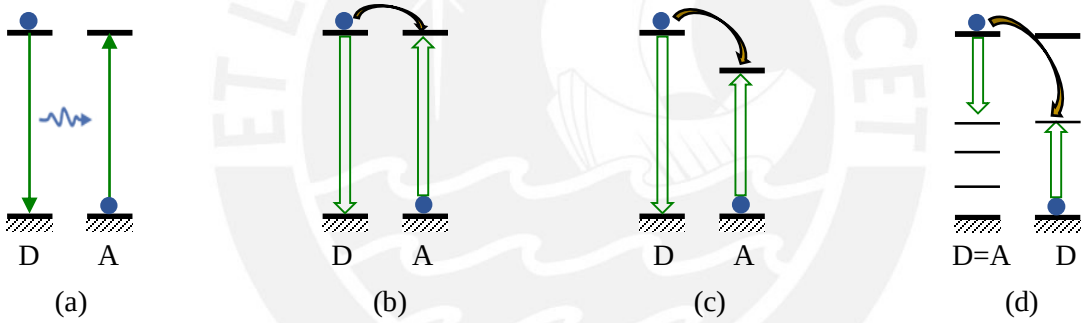

Figure 2.4 Energy transfer process between two ions, where the donor ion transfers its energy to the acceptor ion. Radiative resonant transfer (a), non-radiative resonant transfer (b), phonon assisted non-radiative energy transfer (c) and cross-relaxation [33].

Resonant radiative energy transfer involves the promotion of the donor from the ground state to an excited state by the absorption of the excitation energy. Afterwards, the donor is relaxed to the ground state and transfers its absorbed energy to the acceptor. The acceptor absorbs the energy of the donor and emits its own photon energy. In the case of the non-radiative energy transfer, the donor emits shorter wavelengths that overlap with the absorption spectrum of the acceptor; excitation will jump from donor to the acceptor without the emission of photons. The probability of energy transfer from the donor to the acceptor (Equation 2.1) was described first by Förster and then extended by Dexter [34,35]

$$P_{DA}(R) = \frac{2\pi}{\hbar} |< DA^* | H_{DA} | D^*A >|^2 \int gD(E) gA(E) dE \qquad 2.1$$

Here, $D^*A >$ and $< DA^*$ are the initial and final state, respectively. H_{DA} represents the donor-acceptor interaction and the integral represents the spectral overlap between the donor and acceptor. High energy transfer probability will take place when the overlapping and the Hamiltonian interaction of the donor and the acceptor are strong. H_{DA} contains two important terms. The electrostatic interaction which depends on a series of multipole-multipole terms is described by Förster and the electron exchange is shown by Dexter.

Förster described the dipole-dipole interaction and found a relation between the energy transfer (P_{DA}) and the distance (R) between the ions by the following equation [34]:

$$P_{DA}(R) = \frac{1}{\tau_S} (\frac{R_0}{R_{DA}})^6 \qquad 2.2$$

Here, τ_S is the lifetime of the donor ion, R_{DA} the distance between the two ions and R_0 is the critical Förster transfer distance. As this process involves dipole-dipole (Coulomb) interaction it has low influence at distances large than 100 nm but still larger than the Dexter mechanism.

Dexter extended the work of Förster for the case of multipole and exchange interactions and he described the electric multipolar interaction with equation 2.3:

$$P_{DA}(R) = KJexp(-2R_{DA}/L) \qquad 2.3$$

Where K and J are constants determined by the interaction between the orbits involved in the energy transfer process and by the spectra overlap of the activator ion. L is determined by the van der Waals radii. Since this process involves exchange of electrons, it may dominate at short distances.

Cross relaxation occurs when the donor transfers only part of its energy to the acceptor ions. Therefore, the energy transfer occurs in more than one single step. When the distance between ions is large, the energy transfer has low rate giving a low luminescent of the ions. Cross relaxation usually occurs in materials doped with lanthanides. It also produces the quenching phenomenon, which acts differently in every REs. In this master, concentration quenching effect was found to occur at terbium concentrations higher than1.5 at%.

d) Impact ionization mechanism

Impact ionization is a phenomenon that produces electron-hole pairs via band-to-band or band-defects. It takes place in the presence of a high electric field when high energy carries collided

with the lattice. The starting carrier could be either a free electron or a hole and it transfers its energy to a second carried confined in an impurity [36][37]. Impact ionization involves the participation of electrons with high kinetic energy (hot electrons). The latter gains a considerable amount of energy under very high fields. Rare earth centers can be ionized by the hot electrons by different manners: direct impact, indirect ionization and field ionization [36].

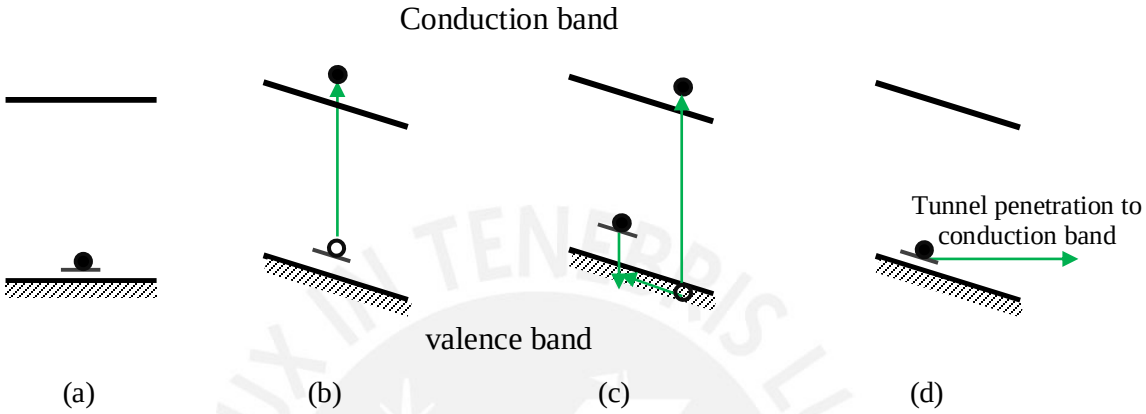

Figure 2.5 Ionization of a donor activator center. Center in ground state (a), ionization by direct impact (b) indirect ionization by prior generation of electron-hole pair (c) and field ionization (d) [36].

Ionization of a donor activator center can occur in the following way. First the center in considered to be on the ground state Figure 2.5 (a). The center can be ionized by direct impact with a hot electron (Figure 2.5 b). The hot electron can excite the host matrix and afterwards, the host matrix transfers its energy to the center (Figure 2.5 c). The center can also be transferred directly to the conduction band, without transfer of energy by the host matrix.

2.4 Applications of RE doped wide bandgap semiconductors (EL devices)

RE doped wide bandgap semiconductors are good candidates as luminescent materials for the fabrication of EL devices. The emission of light can be generated by two ways: radiative recombination of electron-hole pairs or excitation of the ions atoms with high energy electrons. EL devices can be classified into two groups according to the applied current (AC or DC). Alternating current thin film electroluminescence devices (ACTFEL) and direct current thin film electroluminescence (DCTFEL) devices. In the following section, the structure and work principles of both devices will be described.

2.4.1 Devices structure

EL devices are composed of two electrodes, one opaque and the other transparent in order to allow the emission of light out of the device. Furthermore, the device consists of an active layer,

HTL and/or ETL for DC and insulating layers for AC. Table 2.3 summarizes the principal properties of the electrodes and insulator layers that will influence in the operation of the EL devices.

Table 2.3 Physical properties of metals, TCO and insulator layers of the EL devices[1,38–40].

Materials	***Resistivity (μΩcm)***	***Reflectance (%)***	***Melting point (°C)***	***Thermal expansion coefficient (10^{-6}/°C)***
Al	2.71	91-92	660	23.1
Mo	5.47	54-59	2623	4.8

	Transmission (%)	***Bandgap (eV)***	***Refractive index***	***Resistivity (Ωcm)***
ITO	95	3.7	2	1.1×10^{-3}
ZnO:Al	90-95	2	2	1.1×10^{-3}

	Dielectric constant	***Dielectric field ($\times 10^8$ V/m)***
Al_2O_3	8-9	5-8
Si_3N_4	8	6-8
TiO_2	60	0.2

In the case of DC, the opaque electrode injects electrons to the device and the transparent electrode injects holes. Typically, in the case that the active layer is a WBG semiconductor, when DC current is applied to the device, the injected electrons and holes cannot reach the active layer due to the high difference of the electrodes' work functions and the offset of the bands of the active layer. One possibility to improve the injection of electrons and holes is matching the work function by using HTL and ETL. These devices will emit light when a driving voltage in the order of the bandgap of the active layer is applied.

In the case of AC, the electrodes are used to apply a high driving voltage in order to accelerate electrons from the interface insulator/active layer states to the active layer. Insulating layers prevent the breakdown of the active layer due the high voltage applied [17]. These measurements must be performed under pulses of short duration in order to prevent an increase of energy of lattice temperature [36]. The AC driving voltage for AlN:Er and AlN_xO_y:Tb are around 70 V and 170 V, respectively under frequency of 1 MHz [17][41].

The conventional structure is usually deposited on a transparent substrate and finished with the metal electrode. Typical, transparent and metal electrodes are indium tin oxide (ITO) and

aluminum, respectively. The electrode at the side of the substrate must be a transparent conductive oxide (TCO) to allow the emission of the luminescent light through the substrate. In the inverted structure, the transparent and metal electrodes exchange their position, allowing the use of opaque substrates such as silicon and, therefore, opening the possibility of a heat treatment during the production process of the devices. In the inverted structure, the light is emitted in opposite direction to the substrate. Typical conventional and inverted ACTFEL and DCTFEL devices are showed in Figure 2.6.

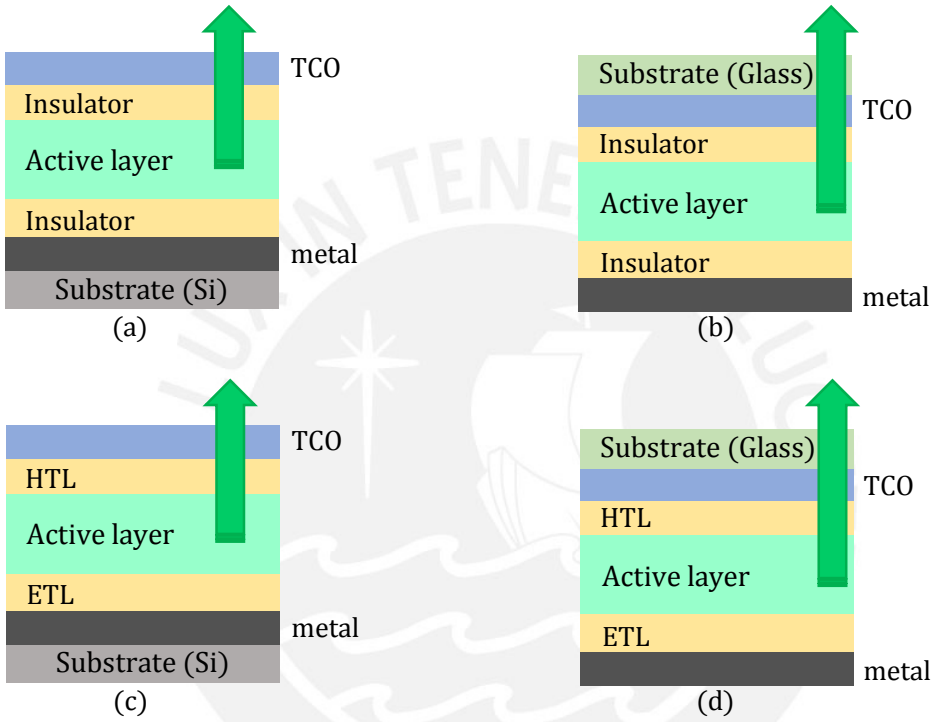

Figure 2.6 Structure of an inverted (a) and conventional (b) ACTFEL devices. And an inverted (c) and conventional (d) DCTFEL devices. The light emission for the inverted EL devices will be in opposite direction of the opaque substrate, while in the conventional case is through the glass substrate.

a) Active layer

The active layer must have a large bandgap which allows the emission of the light in the visible region and UV. In the case of the DCTFEL devices, the active layer should be semiconducting in order to match its work functions with HTL and ETL layers. In the case of ACTFEL devices, the active layer has to withstand high electric field of around 170 V/m without electric breakdown. It also must behave like an insulator below the threshold voltage of luminescence [38]. Common active materials for ACTFEL are wide bandgap semiconductors doped with rare earths such as e. g. AlN:Tb and GaN:Er [16][11]. In the case of DCTFEL devices, organic material is typically employed [42].

b) Transparent conductive oxide (TCO) electrode.

Important characteristics of TCOs include transparency and conductivity as high as possible in order to allow the emission of light and an efficient carrier transport, respectively. A typical electrode in EL devices is ITO, which has a transparency of around 95%. However, it loses its properties at high temperature (see Table 2.3). Another important TCO is the aluminum-doped zinc oxide (Al:ZnO).

c) Metals

Required properties of metals are their low resistivity, good adhesion to the insulating layer and low costs. In the case of the conventional EL devices, aluminum is a good candidate since it is a low cost material. For the case of inverted devices, a good electrode is molybdenum (Mo), since it has a close work function (4.53 eV, 100) than the Al (4.2 eV, 100) [43]. However, the values of the work function will depend on the crystal orientation of the metal [43]. The advantage of Mo over Al, is its high melting point of 2623 C, opening the possibility of heating the device and, therefore, improve the luminescence of the active material [11][31]. Table 2.4 shows a summary of the Al and Mo work functions for different crystal orientations. Work functions of the HTL and ETL suitable for using a-AlO_xN_y:Tb are also included.

Table 2.4 Work function of the ETL, HTL and metals suitable for the DCTFEL devices using a-AlO_xN_y:Tb as active layer [43–48]**.**

	Materials	Work functions (eV)
Electrodes	Al	4.2 (100) , 4.06 (110), 4.26 (111) [43]
	Mo	4.53 (100) , 4.36 (112), 4.95 (110) [43]
HTL	PEDOT:PSS	48.-5.2 [44]
	WC	5.12 [45]
	WO_3	5.6 [46][47]
ETL	ZnO	4.1[48]
	Ca	2.87 [43]
	Sm	2-7 [43]

d) Insulator

Insulator materials should have high dielectric field and dielectric constant to protect the active layer from avalanche breakdown due to the high electric field (see Table 2.3). However, for most of the insulator materials high dielectric constant results in a low dielectric field. Nevertheless, there are some exceptions like Al_2O_3 and Si_3N_4. Insulators also prevent the direct flow of electrons from the electrode to the active layer and provide interface states at the insulator/active

layer interface, in order to give the electrons, the possibility to tunnel into the conduction band of the active layer.

e) Hole and electron transport materials

HTLs have the function of assisting the injection of holes from the electrode anode to the conduction band of the active layer. While, ETLs assist the injection of electrons from the cathode to the valence band of the active layer. Election of HTL and ETL are chosen according to their work function which should match the band offsets of the active layer. Zinc oxide (ZnO), calcium and samarium are good candidates as ETL. Wolfram carbide (WC), wolfram trioxide (WO_3) and the polymer poly(3,4-ethylenedioxythiophene) polystyrene sulfonate (PEDOT:PSS) are good candidates as HTL. Theoretical values of the work functions of these material are presented in Table 2.4.

2.4.2 Working principles

a) AC device

Figure 2.7 shows the working principle of the ACTFEL devices. When a high electric field is applied through the ACTFEL device, electrons from the interface insulator/active layer tunnel into the conduction band of the active layer (injection). Afterwards, they are accelerated across the active layer (transport). The accelerated electrons create electron-hole pairs which can recombine radiatively through a luminescent center. Electrons can also excite the luminescent centers by impact excitation leading to the activation of the luminescent center [49].

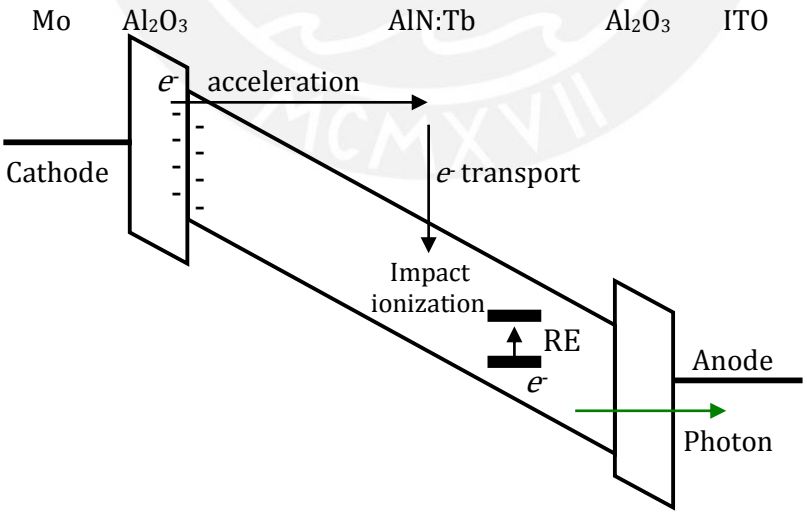

Figure 2.7 Working principle for the ACTFEL devices. Electrons from the interface insulating/active layers are accelerated into the bandgap of the active layer. Light emission is observed because of the impact ionization process [49].

b) DCTFEL device

When DC current is applied through the electrodes of Figure 2.8. The following sequential process happened. Electrons are injected from the cathode (metal) to the ETL and then reach the conduction band of the active layer, while holes are injected from the TCO to the HTL and then to the valence band of the active layer. Electron-hole pair recombines radiative and nonradioactive. The radioactive process excites the Tb ions and light emission is observed. ZnO could be a suited ETL for the case of AlN:Tb. WC in combination with WO_3 could be good candidates as HTL.

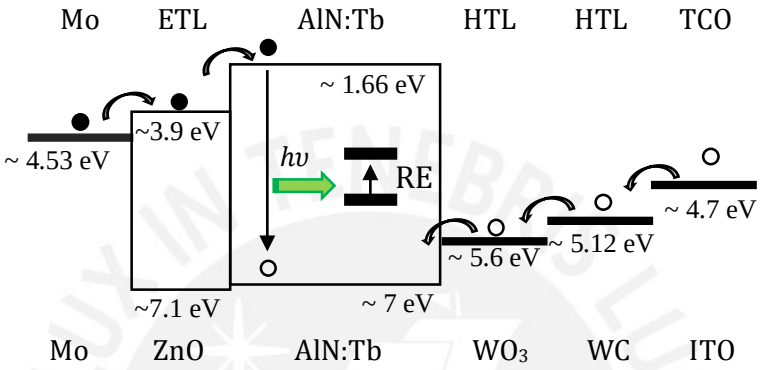

Figure 2.8 Operation principle for the DCTFEL devices. Electrons (black circles) are injected from the metal electrode to the active layer and holes (white circles) are injected from the transparent electrode. Once, electrons and holes reach the minimum and maximum of the conduction and valence bands, respectively, they recombine and afterwards transfer its energy to the rare earths.

3. Deposition and analytic techniques

In this section the background and basic principles of the deposition and analytic techniques will be presented. The growth of the layers was done using radiofrequency (RF) and direct current (DC) magnetron sputtering systems. The structural characterization was performed using X-ray diffraction (XRD). The morphology of the samples was studied by scanning electron microscopy (SEM). Chemical composition was investigated by energy dispersive X-ray spectroscopy (EDS) and X-ray photoelectron spectroscopy (XPS). Vibration modes were studied by Fourier infrared transform spectroscopy (FTIR). Finally, the luminescence properties were performed by photoluminescence (PL), cathodoluminescence (CL) and electroluminescence (EL). Table 3.1 summarizes the information that each analytic technique provides.

Table 3.1 Analytic techniques used for investigating of the thin films [50]**.**

Technique	***Particle in/ Particle out***	***Information obtained***	***Additional information***
EDS	Electron/electron	Quantitative elemental analysis	Depth: depends on the acceleration voltage, Elements: from Boron to Titanium
SEM	Electron/electron	Surface morphology	Depth: from few nm to few µm
XRD	Photon/photon	Crystal structure, grain size, phase identification, texture	Depth: usually few µm
FTIR	Photon/photon	Vibrational frequencies of chemical bonds	Depth: from µm to 10 nm
XPS	Photon/photon	Elemental analysis of surfaces, Chemical states of the elements	Depth: 0.5-10 nm. Elements: all elements except He and H_2
PL	Photon/photon	Analysis of luminescent center, chemical composition, impurities	Depth: 0.1-3 µm
CL	Electron/photon		Depth: depends on the electron beam energy (1-40 keV)
EL	Current/photon	Terbium emission	Direct or alternate current can be applied depending on the structure of the devices.

3.1 Deposition techniques

3.1.1 Radiofrequency (RF) and direct current (DC) magnetron sputtering

Basic principles of RF and DC magnetron sputtering technique.

Sputtering is a deposition technique to grow a wide range of materials, compounds or individual materials. In this technique, atoms from the surface of a target are bombarded by ionized particles (ions) from a gas with high kinetic energy. In the collision event between atoms and ions, some atoms acquire enough energy to escape from the surface. Finally, these atoms are directed to a substrate where they are condensed and form a film.

The common gas used in sputtering is argon, since it is inert and inexpensive. When the gas is reactive, the ionized atoms chemically combine with the atoms of the gas giving as a result a material with different properties compared to the target. This technique is known as reactive sputtering. Common reactive gases are oxygen, nitrogen or hydrogen. I. e., if the sputtering atmosphere consists only of Ar atoms, a silicon layer will be grown on the substrate. When oxygen is added to that process, silicon dioxide (SiO_2) is obtained and in the case of nitrogen is added, silicon nitride (Si_3N_4) can be produced. Hydrogen is typically used for passivation of the dangling bonds as is well known in the case of silicon (*a*-Si:H) [51].

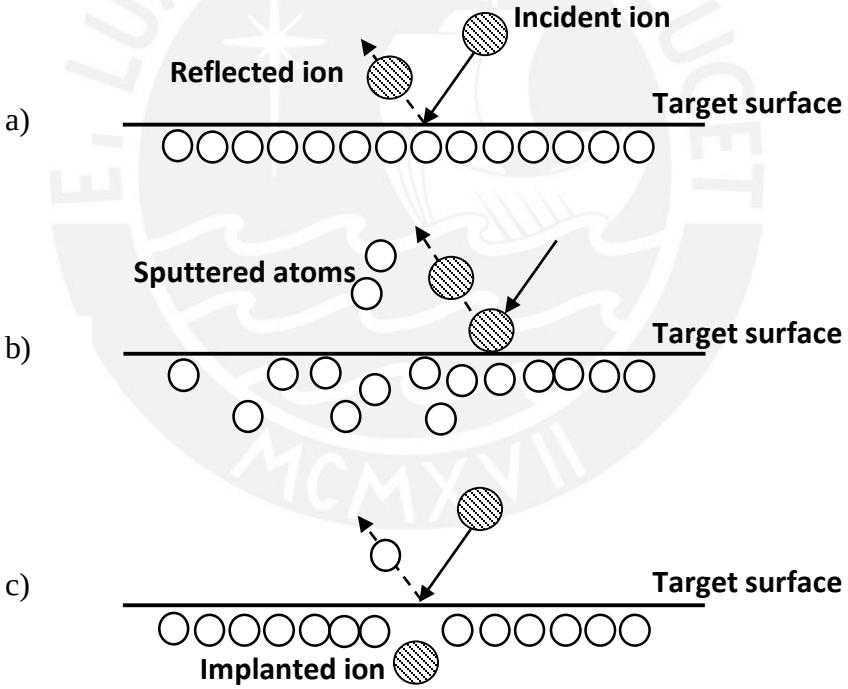

Figure 3.1 Regimes of the sputtering process. Threshold regime (~50-300 eV) (a), very low energy regime (~100 eV) (b) and high energy region (~10-100 KeV) (c) [52]**.**

The sputtering process can be characterized by the sputter yield Y (see Equation 3.1). It is defined as the ratio of ejected atoms of the target surface due the bombardment with ionized ions.

$$Y = \frac{sputtered\ atoms\ removed}{incident\ ions} \qquad 3.1$$

The sputter yield depends on different factors such as the energy and the angles of the incident ions and also the properties of the target.

The principle factor of the sputter yield is the energy of the bombarding ions, which can be divided in three ranges [52][53]. In the first range, the threshold sputtering energy is low (<100 eV). Since the energy is less than the surface binding energy, the ions only eject weakly bonded surfaces atoms. The second range corresponds to the very low energy sputtering (~100 eV), the ions energy is higher than the binding energy of the target atoms and, therefore, the ions can eject atoms of the target reaching the best sputter yield. In the third range, collision cascades (~10-100 KeV) are originated. Even though, the ion energy is high, the sputter yield decreases, since ions are implanted into the target (see Figure 3.1).

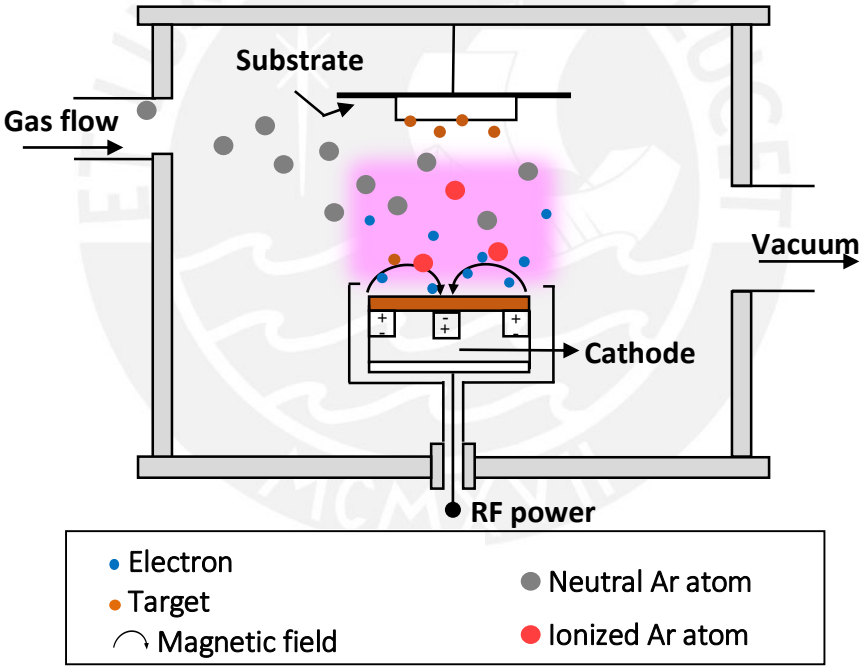

Figure 3.2 Basic scheme of the RF magnetron sputtering process. Ar atoms are introduced in a high vacuum sputtering chamber and subsequently ionized using a high frequency electrical field of 13.56 Mhz. The ionized atoms bombard the surface of the target and extract some atoms, which are directed to the substrate. The magnetic fields confine the electrons close to the surface of the target and it does enhance the deposition rate.

Sputtering is based in the DC basic model, which was later improved by the using of magnetrons and radiofrequency sources (see Figure 3.2). Direct current (DC) sputtering consists of two electrodes: the negative electrode where the target is placed and a positive electrode where the substrate is placed. The source of ions is generated by applying an electric field between the two

electrodes in a gas atmosphere at low pressure (10^{-3} mbar). These ions are impinging on the target, where their electrical charge is neutralized. DC is suitable for metals, but for insulating materials, the positive charges of the ions will accumulate on the surface of the target repelling the bombarding ions and afterwards stopping the sputtering process. This problem is solved by applying frequencies in the range from 10°kV to 100°kV, across the electrodes, alternating the polarization of the target (RF sputtering). At these frequencies, the build-up of charges at the target surface is unprovable, due the short time. In this case, the electrons are oscillated in the RF source and remain in the plasma increasing the probability of ionization [54]. The RF alternates the polarity of the target. In the positive half cycle, electrons are attracted to the target and in the negative half cycle ions will be attracted. A magnetic field is also employed in order to raise the deposition rate by the confinement of the electrons close to the target surface. Due the presence of the magnetic field, the paths of the electrons are helicoidally, increasing the probability of ionization process and the ion density.

Working principle of the sputtering system used in this thesis

The used sputtering equipment is a face-down system equipped with a vacuum chamber, magnetrons, as well as a substrate-holder, RF and gas sources. The chamber is evacuated using a combination of a mechanical and a turbo-molecular pump. The target is fixed on the surface of the magnetrons and the substrates in the substrate-holder. The cooling system is used in both, the substrate holder and the magnetron, in order to protect the magnets and to ensure the amorphous state of the layers. Figure 3.3 shows an image of the vacuum chamber of the sputtering system used for the deposition of the active layer.

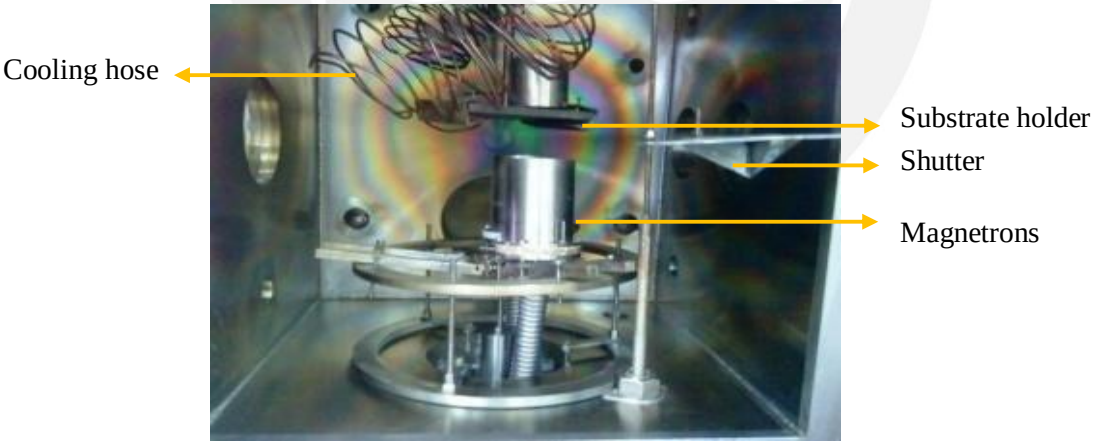

Figure 3.3 Image of the vacuum chamber of the sputtering equipment used for the deposition of the active layers. The image shows two of the magnetrons and the substrate- holder.

The deposition of samples by sputtering can be done by the following steps. First, the generation of a high vacuum in the order of 10^{-6} mbar before the deposition in order to ensure an atmosphere without unwanted elements such as the oxygen and, therefore, avoid the incorporation of these undesired elements in the thin film. When a high vacuum is reached, the

inert gas is introduced into the vacuum chamber and afterwards, an electric RF-field with a frequency around of 13.56 Mhz (for the case of AlN) is applied through the target. The electric field ionizes the neutral gas resulting in the formation of plasma. The plasma is support by two ways: through the ejection of the valence electrons due the high electric field and due the acceleration of the free electrons through the inert gas. The ions coming from the source impinge on the target and thereby transfer their energy to the target atoms. The atoms with enough energy to leave the surface of the target are expulsed and directed to the substrate, where they condense and form a thin film. More experimental details are shown in subsection 4.1.1.

3.2 Characterization techniques

In the following part, the characterization techniques briefly will be described. A detailed theory of techniques can be found in the following books: [50,55–59]. When an energetic radiation interacts with matter different physical phenomena can occur. Secondary effects, such as Auger and backscattered electrons are produced, electrons are transmitted or scattered, and X-rays as well as cathodoluminescence are generated (see Figure 3.4). When electron-matter interaction occurs with a loss of energy, the energy loss is transferred to the matter in different ways, as thermal vibration, excitation or ionization. In the case of infrared radiation, its molecules are excited producing vibration between their atoms. Visible light promotes the electronic transition from the valence band to the conduction band and X-rays can induce ionization.

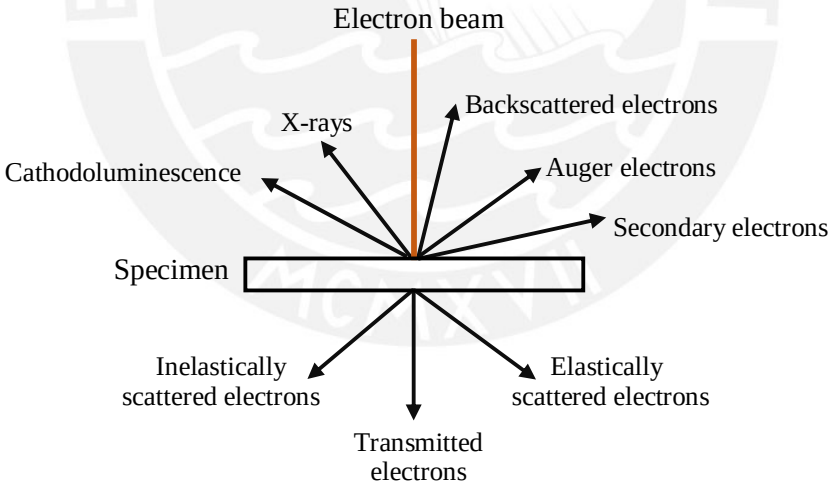

Figure 3.4 Schematic drawing of energetic radiation-matter interaction, showing the different emitted signals after their interaction with matter [56]**.**

3.2.1 Scanning electron microscope (SEM)

The scanning electron microscope (SEM) allows the observation and analysis of the microstructure at the surface of a specimen. When an electron beam impinges into a sample, the electrons interact with its atom and their electrons (see Figure 3.4). Secondary electrons (SEs)

and backscattered electrons (BSEs) can contribute to the formation of the images. SEs are produced by inelastic scattering, where the incident electrons transfer kinetic energy to the electrons in the atoms of the sample. If the electron in atoms reaches sufficient kinetic energy, it can escape from its orbitals and leave the sample surface. BSEs are produced by elastic scattering, in this case, electrons are scattered backward by atoms of the specimen losing a part of their energy.

The volume penetrated by the incident beam exhibit a teardrop shape (see Figure 3.5). Initial scattering occurs at low angles and spreads slowly at the beginning. As the electrons are several times scattered the beam broadens. SEs electrons have low energy, less than 50 eV. Because of the low energy of SEs, they are attracted easily by the charge (+300 V) of the Faraday cage of the detector. Therefore, the image is formed principally by SEs [55].

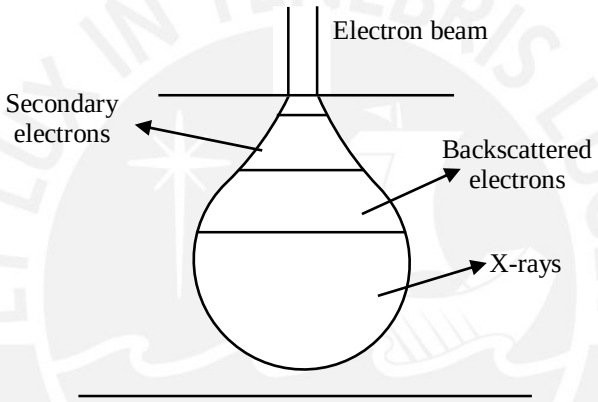

Figure 3.5 Illustration of electron penetration in the specimen. Auger electrons, SEs, BSEs and X-ray signals are shown.

SEM provides high resolution images due their small wavelengths. Ernst Abbe found that resolution of an optical lens illuminated with parallel beams of light depends on the wavelength of the illumination source and is described by Equation 3.2 [56].

$$\delta = \frac{0.612\,\lambda}{n\,sin\alpha} \qquad 3.2$$

Where, δ is the resolution, λ is the wavelength of the irradiated electrons, n is the refractive index of the medium between the source and lens, and α is the aperture (half-angle) of the lens. The term $n\,sin\alpha$ is known as the numerical aperture (NA). The distance over which the object and image are in focus is defined by the depth of field (d) and depth of focus (D), respectively. Both parameters are related by the following equation:

$$D=M^2d \qquad 3.3$$

Where, M is the magnification and d depends on the resolution and the angle between the objective aperture and the focal point.

The resolution of SEM images depends on several factors. Spot size, beam current, depth of field and acceleration voltage. In a SEM measurement, the principle variable adjustable is the acceleration voltage. At low acceleration voltage (<5 kV) the beam-specimen interaction occurs very close to the surface, providing good surface detail, but poor resolution. High acceleration voltage (15-30 kV) penetrates below the surface and the electron carries information from that region, providing high resolution images but less detail information compared to images obtained at low acceleration voltage [57].

Experimental setup

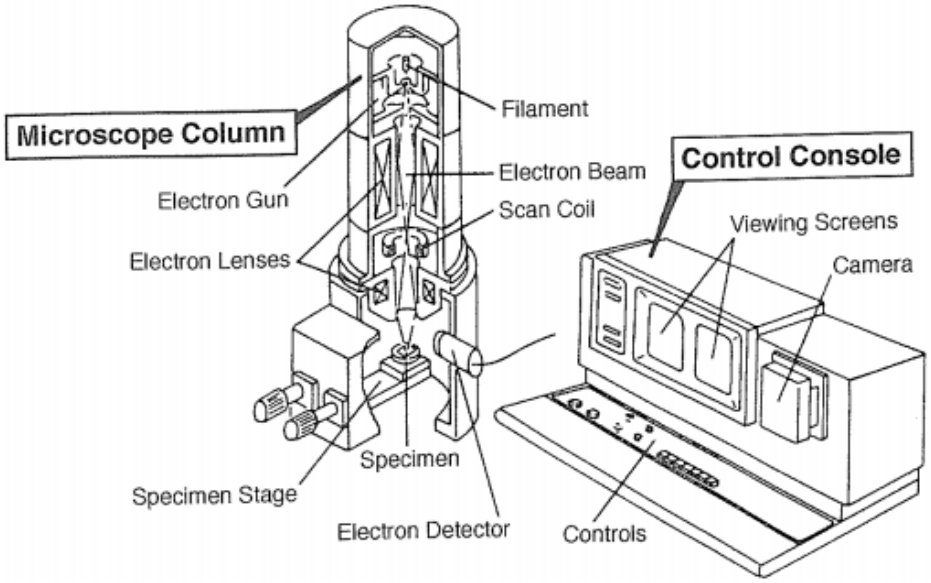

Figure 3.6 Principal components of the SEM [57]**.**

A SEM equipment consist of an electron gun, electromagnetic condenser system, objective lens and a detector (see Figure 3.6). The electron gun is located on top of the column maintained under high vacuum. The gun could be a thermionic emission gun. The most common are the tungsten filament and a lanthanum hexaboride single crystal (LaB6), these gun sources generated a current density of 5×10^4 Am^{-2} and 1×10^6 Am^{-2}, respectively. Field emission gun produces a current density of 1×10^{10} Am^{-2}[56]. The best gun source is the field emission gun due their high brightness, long lifetime (>1000 h) and low energy spread (< 1 eV) [57]. The electrons of the gun are focused into the condenser lens, pass through the objective lens and reach the specimen stage. Finally, backscattered or secondary electrons generate a point to point image on the screen.

Basic principles of EDX

Energy dispersive X-ray spectroscopy (EDX) uses X-rays to identify chemical elements, from Boron to Titanium [59]. When atoms are irradiated with X-rays, electrons in the inner shell of an atom can be excited to a higher energy state leaving a vacancy. This vacancy is further filled by an electron in the outer shell, thereby releasing energy and emitting X-rays whose energy correspond to the difference between the outer and the inner shell. When the K-shell is filled by an electron from the L-shell, the energy of the atom will decay to the low state (E_L) and the decrease in energy of the excited atom (E_{KL}) will be emitted as K_α X-rays. If the vacancy is filled by an electron from the M-shell, the energy of the atom will decay in a state E_M with lower than E_L and the decrease in energy of the excited state (E_{KM}) will result in the emission of K_β X-rays (Figure 3.7). The intensity of the K_α X-rays is higher than the K_β X-rays, since E_{KL} are higher than $E_{KM.}$

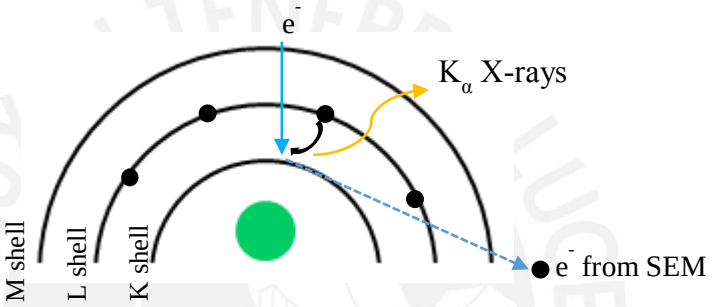

Figure 3.7 Generation of characteristic X-rays. An incident electron from the beam ejects an electron from the K-shell. An L-shell electron fills the vacancy and produces a K_α X-ray.

EDS typically is attached to a SEM equipment. The detector in the EDS is usually a solid state detector, which behaves like the intrinsic silicon [57]. It contains a thin layer of a p-type material, which is coated with gold as electrical contact. When photons are captured in the detector, they produce electrons in the conduction band and holes in the valence band. These electrons and holes can be swept apart by applying a bias. Afterwards, they are collected on the electrodes of the crystal.

3.2.2 X-ray Diffraction (XRD)

Basic principles of XRD

XRD is a non-destructive analytic technique which provides a structural fingerprint of a material. This technique is used to identify crystalline phases, grain size, texturing and stress. A perfect crystal consists of lattice planes separated by a distance d. If X-ray beam is directed to a sample and consequently scattered by the lattices planes (see Figure 3.8) interfere constructively, they satisfy the Bragg equation (Equation 3.4) and a diffraction peak is observed in the diffractogramm.

$$2d_{hkl}\,sin(\theta) = n\lambda \qquad 3.4$$

Where, hkl are the Miller indices of the lattice planes associated with the diffraction, d_{hkl} is the distance between these lattice planes. θ is the incident angle of the beam, λ is the wavelength and n is a constant value.

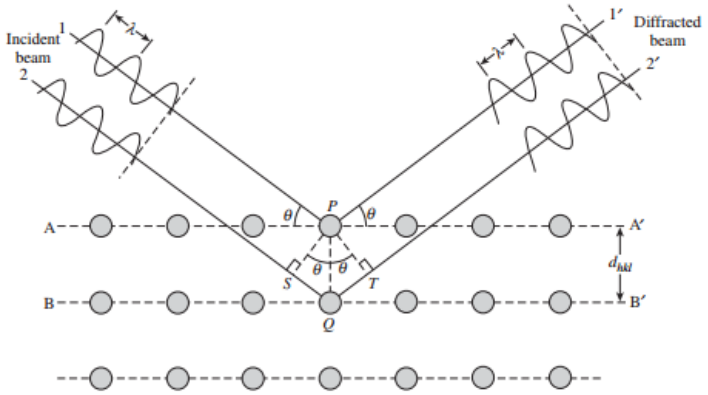

Figure 3.8 Bragg diffraction by lattice planes [60]**.**

Thin films are formed by a huge number of crystalline grains having a distribution of orientation. A diffraction pattern gives several information of that thin film. First, the crystalline phases can be identified by matching the peaks of the diffraction pattern to a reference database, usually with a power diffraction file (PDF). Preferred orientations can be observed, when diffracted peaks are absent, weak or strong in comparison to the reference data. Another important parameter is the grain size which can be calculated using the Scherrer equation [61].

$$d = \frac{K\lambda}{B(2\theta)cos\theta} \qquad 3.5$$

Where, d is the mean average crystal size, K is a constant, λ is the wavelength of the X-rays in nanometers, B is the peak width at half maximum height of the diffraction peak and θ is the position of the peak maximum. The Scherrer equation predicts crystal size correctly only for specimens with crystals without internal strain.

Experimental Setup

The Bragg Brentano configuration consists of the following elements: an X-ray tube, an incident beam optics, Soller slits, a receiving side optics and a detector. The Soller slit consists of closely spaced parallel thin metal plates, which divides the beam into several slightly divergent beams. A continuous beam of X-rays generated in a cathode ray tube by heating a filament are collimated, passes through a Soller slit and then concentrate toward the sample. The electrons with enough energy to remove inner shell electrons from the material are diffracted by the crystalline phases in the material according to the Bragg's law and produce characteristic X-rays. The intensity of

these X-rays passes by a Soller slits and then is collected by the detector as a function of the diffraction angle 2θ and the orientation of the specimen. In the Bragg Brentano configuration, the sample is fixed, whereas the incident (θ) and scattered angle (2θ) varied during the measurements.

In grazing incidence X-ray diffraction (GID), with the aim of retrieve information mainly of the layer and reduce the substrate signal, the sample is fixed at a small grazing incidence angle. GID uses a Göbel mirror (multilayered mirror) with the aim of reduce the divergence of the beam. It is usually situated at the exit window of the X-ray tube and it converts the divergent radiation coming from the source into parallel beam [62]. Penetration depth in the case of AlO_xN_y:Tb, at an incidence angle of 3 ° assuming a density of 4g/cm³ and using a Cu Kα radiation is 3.3 µm.

3.2.3 Fourier transform infrared spectroscopy (FTIR)

Basic principles of IR absorption

FTIR spectroscopy is a non-destructive technique which provides detailed information of a molecule, such as the chemical bonds within the molecule. The infrared radiation falling in the region from 0.7 to 1000 µm, excites vibrational and rotational motions in molecules.

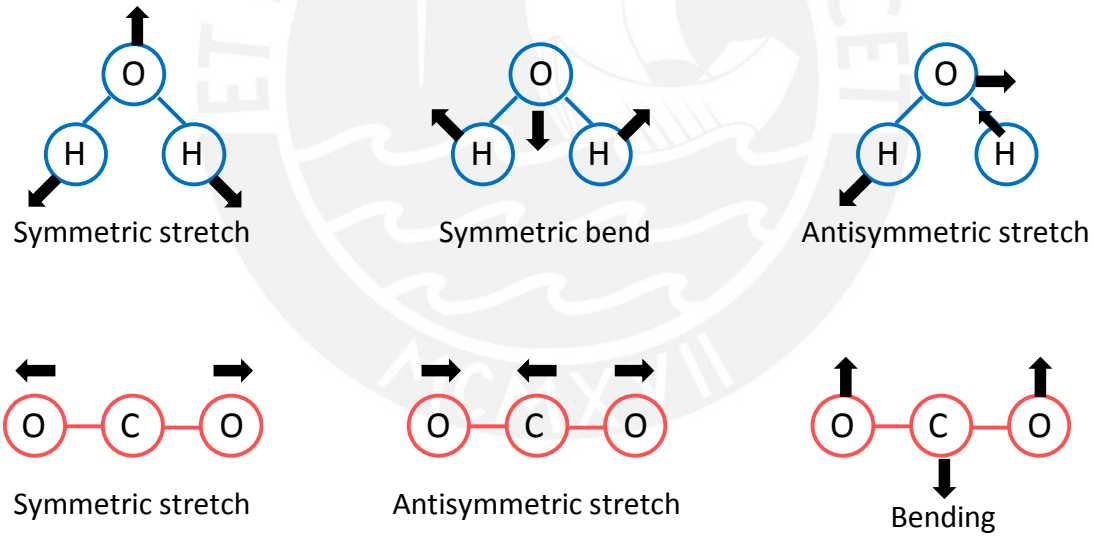

Figure 3.9 Characteristic vibration of water (H_2O) and carbon dioxide (CO_2) [62]**.**

Matter is composed of molecules, which at equilibrium positions are always in vibration. When a molecule is irradiated with a continuous light source in the IR region and the energy of the radiation matches the energy difference between an excited and a ground state, vibrational transitions take place. The energy difference between the excited and ground state is described by the following equation [62]:

$$E_e - E_g = h\nu \qquad 3.6$$

Here, E_e and E_g are the ground and excited state, respectively.

The infrared absorption will occur when Equation 3.6 is satisfied and also two laws apply thereby. The first law requires a change in the vibrational quantum number equal to ± 1 for allowed transitions. The second rule requires a change in accordance with a particular vibration mode of the electric dipole moment of the molecule. In accordance to the last rule, asymmetric modes are allowed while symmetrical vibrations are forbidden because the electric dipole moment is not changing. The symmetrical vibrations are usually active in a Raman spectrum. However, in some special cases, symmetrical vibration also could be observed in IR spectra. A polyatomic molecule experiences several types of vibration and rotation. In Figure 3.9, the characteristic vibration of water and carbon dioxide are presented.

Experimental setup

The basic components of the FTIR spectrometer are: a source of infrared light, an interferometer, the substrate holder and the detector (see Figure 3.10). The main component of the FTIR spectrometer is the interferometer which has a beam splitter and two pairs of mirrors.

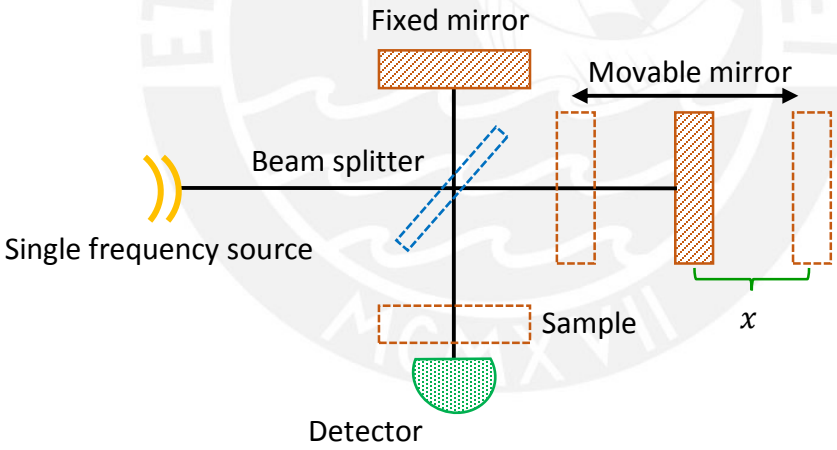

Figure 3.10 Principle components of an FTIR spectrometer.

In the experiment, a broad light source which covers the IR range is directed to a beam splitter, which divides the incoming infrared light into two optical paths: half of the light is reflected and goes to the fixed mirror and the other half is transmitted and sent to the moving mirror. The two beams meet back at the interferometer and are split into two: one goes back towards the source (lost light) and the other goes to the detector. The moving mirror produces an optical path difference (OPD) between the two arms of the interferometer. When the distance from the center of the beam splitter to the fixed mirror and the distance from the beam splitter to the movable mirror are different, the optical path lengths become unequal. This optical path difference (OPD),

also known as retardation is represented by δ. The OPD is $\delta = 2x$ since the light has to travel a distance x to reach the mirror and another distance x to reach the point where the mirror was before being moving. The beam leaving the interferometer passes through the sample, then it is focused on the detector and the detector finally measures the intensity I(x) of the combined IR beams as a function of the moving mirrors displacements x. This is also called interferogram.

3.2.4 X-ray photoelectron spectroscopy (XPS)

Basic principles of XPS

XPS is an analytic surface technique used to detect all elements except hydrogen and helium, since these elements have no core levels. The photoemission process is depicted in Figure 3.11. First, the sample surface is irradiated with characteristics soft X-rays (~1486.6 eV) of a source, hitting the core electrons of the atoms. Second, the sample absorbs the photons and free electrons are emitted with the binding energy E_B (difference in energy between the excited and the neutral atom) below the vacuum level. Finally, the electrons are transported to the surface with kinetic energy E_k defined by the following equation.

$$E_k = h\nu - E_B \qquad 3.7$$

Here $h\nu$ is the energy required to eject electrons from the sample surface and E_B is the energy required to remove the excited electron to the vacuum level.

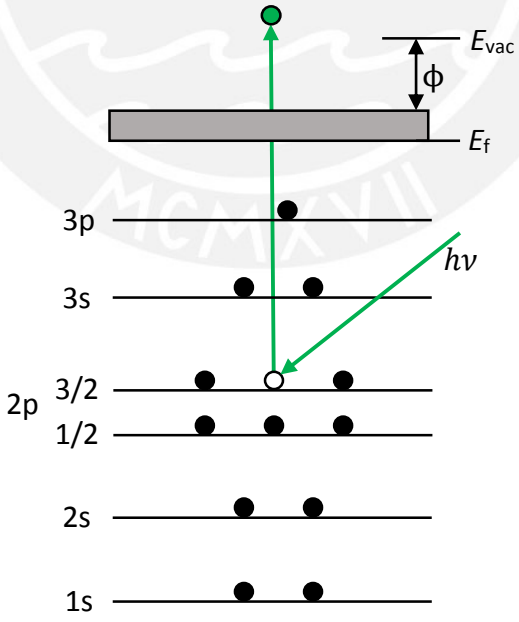

Figure 3.11 Electronic level of an Al atom showing the photoemission process of the 2p level. The Al atom is irradiated with X-ray photons and produce thes emission of a 2p level electron to the surface.

The binding energy can also be expressed in reference to the Fermi level by Equation 3.8.

$$E_k = h\nu - (E_b + \phi) \qquad 3.8$$

Here E_b is the energy required to raise the excited electron to the fermi level and ϕ is the work function of the material, which represents the minimum energy required to bring the electron to the vacuum level.

The electron levels of an atom can be divided in core and valence levels. The core levels are tightly bound to the nucleus, thus, they are not involving in the chemical bonding. The valence levels are only weakly bound to the nucleus, thus, the most probably interactions should be between the valence bands of the atoms given rise the formation of chemical bonds. XPS is surface sensitive because of the short distances that the electrons can travel before they lose energy in collision with the atoms. The flux of electrons emerging without being scattered (I_d) is described by the following equation [50].

$$I_d = I_0^{\frac{-d}{\lambda_e sin\theta}} \qquad 3.9$$

Where, I_0 is the flux of electrons originated at a depth d, θ is the angle of the electron emission, $d/\sin\theta$ is the distance traveled through the specimen at the angle θ, and λ_e is the inelastic mean free path of the electron.

Experimental setup

The experimental setup consists of an ultra-high vacuum (UHV) chamber with a pressure in the order of ($\sim 10^{-8}$ mbar). The UHV is needed to avoid contaminations at the sample surface during the measurements. The UHV chamber is equipped with a substrate-holder, an argon ion sputtering, an X-ray source with high energies to excite core levels, electron lenses, and a hemispherical analyzer system. When the samples are exposed to air, their surfaces are usually contaminated with species such as carbon or oxygen. These unwanted atoms can be removed by sputtering the surface of the sample with Ar ions. However, after the cleaning of the sample, Ar atoms can be detected in the XPS spectrum, thus, will be influenced in the elemental quantification of the sample. Once the sample is cleaned, its surface is irradiated with photons generated from the X-ray source, usually AlK_α (1486.6 eV) or MgK_α (1256.6eV) [50]. The photons are absorbed by the sample and electrons are emitted. The electrons cross the lenses before entering into the analyzer system. The hemispherical shape of the analyzer is suitable to accelerate o retardate electrons at a defined pass energy, it allows a constant absolute resolution in the whole energy range scan [60]. The collected electrons contain usually the contribution of photoelectrons and Auger electron lines.

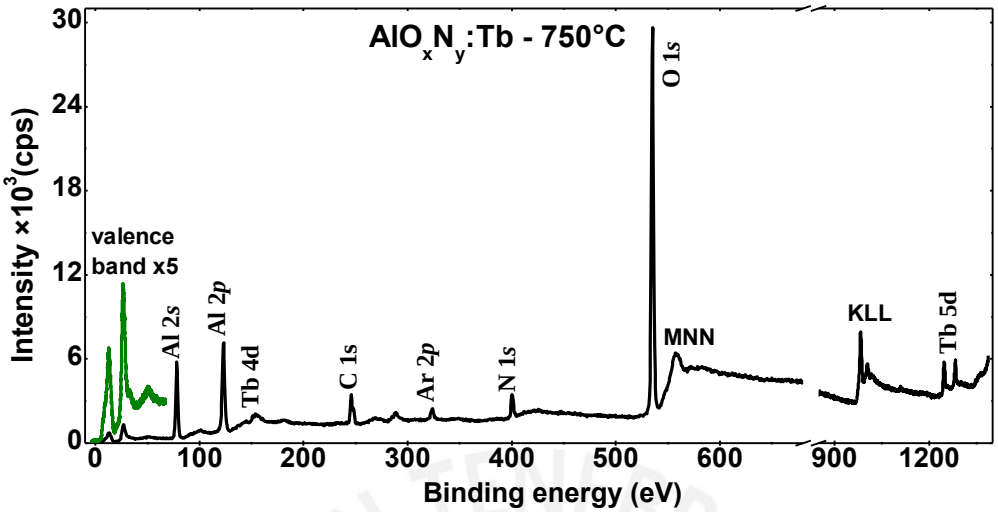

Figure 3.12 Photoelectron spectrum of a-AlO_xN_y:Tb thin film showing the characteristic core levels, the Auger electrons and the valence band. Further details are going to be shown in the later chapter.

Figure 3.12 shows a XPS spectrum of an AlO_xN_y:Tb sample. The spectrum shows clearly the lines of the photoelectrons corresponding to the Al, N, Ar, O, C and Tb core levels [63–65]. The lines of the Auger electron (MNN and KLL) also appear and the valance band is included.

3.2.5 Electroluminescence (EL)

Electroluminescence is a phenomenon produced when an electrical voltage is applied across the electrodes, causing a current to pass through the device [49]. The EL emission mechanism depends on the applied voltage. In the case of AC, above the threshold voltage, electrons are injected from the insulator/active layer interface states into the active layer by tunneling. The injected electrons excite the luminescent center and the host matrix. The excitation of luminesce center are directly excited by hot electrons through impact excitation mechanism [49]. In the case of DC current, holes are injected from the anode to the valence band of the active layer and electrons from the cathode to the conduction band. Light emission is produced when electron-hole pairs recombine and transfer its energy to the luminesce center. Photoluminescence (PL) and cathodoluminescence (CL) generally provide the same spectra as the EL. However, both PL and CL are measured directly on the active layer. These techniques require neither electrodes nor insulators. PL uses light to measure the radiative recombination when a sample is irradiated with a laser. The wavelength of the laser depends on the host matrix and the luminescence center. In the case of the CL, an electron beam excites the specimen and causes the emissions of photons in the ultraviolet, visible and near infrared range.

4. Methodology and experimental details

In this section, the experimental details of the deposition and analytic techniques of the thin films are presented. Amorphous SiC and AlN host matrices doped with terbium were first intended to be deposited. XRD measurements confirm the amorphous nature in the as deposited state of the samples. EDX reveals that the un-doped and terbium doped layers present a high concentration of oxygen (~40 at %). Therefore, the un-doped samples will be referred to as amorphous silicon oxycarbide (*a*-SiC_xO_y) and amorphous aluminum oxynitride (*a*-AlO_xN_y). The doped layers will refer as amorphous silicon oxycarbide (*a*-SiC_xO_y:Tb) and aluminum oxynitride (*a*-AlO_xN_y:Tb) doped with terbium.

Un-doped and terbium doped *a*-AlO_xN_y and *a*-SiC_xO_y thin films were grown by radiofrequency (RF) magnetron sputtering in the material science laboratory at the PUCP. Insulators, HTL, ETL and electrodes for the conventional and the inverted EL devices were produced by RF and DC magnetron sputtering using the LA 440 equipment in the IMN in Ilmenau. The structuring of the inverted devices was performed at Meitnerbau in Ilmenau. The RF magnetron sputtering system at PUCP consist of a vacuum chamber with three flexible magnetrons in which targets with a diameter of 51 mm are fixed. The substrate-holder is located on the top side of the chamber. The sputtering system at IMN is equipped with one RF, two DC sources and one inverse sputter etching system that are located in the bottom of the chamber. Targets of 90 mm of diameter are fixed on the magnetron. A rotatable substrates-holder with for substrate positions are fixed at the top of the chamber, thus, in each process, four set of samples can be coated resulting in huge production output of samples. The advantage of the last point is the possibility to prepare several devices in one day, where every device consists of different layers.

4.1 Deposition of the thin films.

4.1.1 Deposition of the un-doped and terbium doped a-AlO_xN_y layer.

Un-doped and terbium doped *a*-AlO_xN_y and *a*-SiC_xO_y thin films were grown on crystalline silicon (*c*-Si, 100) substrates by radio frequency magnetron sputtering using AlN (with oxygen impurity below 90 ppm), SiC (with nitrogen as main impurity and less than 10 ppm) and terbium (5N purity) targets. Ar/N_2 (1:0.2) and Ar/H_2 (1:0.1) atmosphere mixture were used for the deposition of the un-doped and terbium doped *a*-AlO_xN_y and *a*-SiC_xO_y:H, respectively. Hydrogen was incorporated during the deposition process of the *a*-SiC_xO_y in order to passivate the dangling bonds. Due the flexible geometry of the magnetrons different Tb concentrations in the active layers are expected. Figure 4.1 shows an image inside the vacuum chamber during the deposition process. The magnetron with the AlN and Tb targets are at the bottom. The substrate holder with the glasses substrates are located at the top. The color green around the glass is due the emission of the terbium.

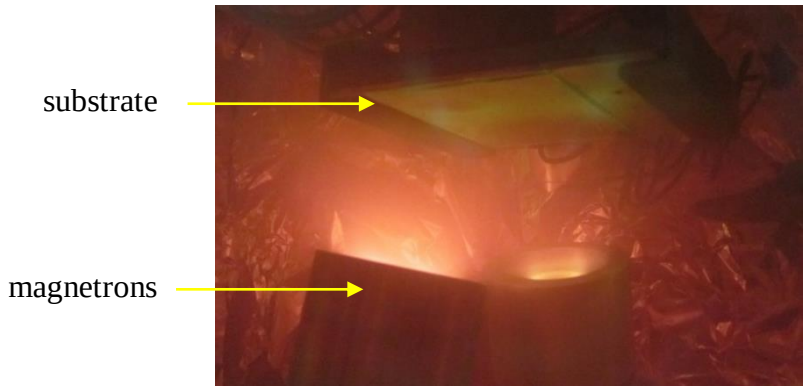

Figure 4.1 Image inside of the vacuum chamber during the deposition process of the a-AlO_xN_y:Tb thin film. The green luminescence of the Tb can be observed by naked eye.

The background pressure before the deposition process was smaller than 5×10^{-6} mbar. The work pressure was set to 1.5×10^{-2} mbar and 1.0×10^{-2} mbar for the *a*-AlO_xN_y:Tb and *a*- SiC_xO_y:Tb, respectively. The distance between the target and the substrate was fixed to 55 mm. The substrate-holder as well as the magnetrons were cooled down with a constant water flux at 12 °C in order to ensure the amorphous state of the sample. The deposition conditions for the samples are summarized in Table 4.1.

Table 4.1 Deposition parameters of the active layer

Layer	*Target*	*Source*	*Ar- N_2 - H_2 sccm*			*P_{base} (mbar)*	*P_{work} (mbar)*	*Power (W)*	*Deposition rate (nm/s)*
a-AlO_xN_y	AlN	RF	10	2	-	3.5×10^{-6}	1.5×10^{-2}	100	0.028
a-AlO_xN_y:Tb	AlN/Tb	RF	10	2	-	3.2×10^{-6}	1.5×10^{-2}	100	0.028
a-SiC_xO_y	SiC	RF	40	-	2	4.2×10^{-6}	1.0×10^{-2}	100	0.014
a- SiC_xO_y:Tb	SiC/Tb	RF	40	-	2	4.1×10^{-6}	1.0×10^{-2}	100	0.014

4.1.2 Preparation of the EL devices and deposition of the insulator HTL, ETL and electrodes.

For the case of conventional devices, the ITO was sputtered from a commercial source and the PEDOT:PSS polymer was grown by spin coating.

Deposition parameters of the insulating layers, HTL, ETL and electrodes of the conventional and inverted DCTFEL and ACTFEL devices grown by the LA440 sputtering system are shown in Table 4.2. A base pressure less than 8×10^{-7} mbar was used for the deposition of all the thin films. In the case of the WO_3 and ITO, oxygen gas was added to the deposition process in order to

ensure the stoichiometry of these layers. The thin film thickness for the HTL and ETL are fixed to 10°nm. The thickness of the insulating layers was varied from 80 to 150°nm. The thickness for the case of electrodes was from varied from 150 to 200°nm.

Table 4.2 Deposition parameters of the HTL, ETL, insulating layers and electrodes of the EL devices.

Layer	*Target*	*Source*	*Gas Ar / O_2 sccm*		*Deposition rate (nm/s)*	*P_{work} (mbar)*	*Power (W)*	*Thickness (nm)*
Al_2O_3	Al_2O_3	RF	80	-	0.12	8.7×10^{-3}	200	100/80
Si_3N_4	Si_3N_4	RF	80	-	0.33	8.8×10^{-3}	200	150/100
Mo	Mo	DC	80	-	1.79	8.5×10^{-3}	200	200
Al	Al	DC	80	-	1.56	8.8×10^{-3}	200	200
ZnO	ZnO	RF	80	-	1.11	8.5×10^{-3}	200	15
WO_3	W	RF	20	1	1.59	4.0×10^{-3}	100	10
WC	WC	DC	80	-	1.11	8.5×10^{-3}	200	10
ITO	ITO	RF	80	1	1.8	8.7×10^{-3}	200	150/200
AZO	AZO	DC	80	-	1.47	8.8×10^{-3}	200	150/200

a) DCTFEL devices.

The fabrication of the conventional structure DCTFEL devices were performed in the following steps: First, ITO electrode was grown on glass substrates. Then, one edge of the ITO was etched from the glass in order to grow the metal electrode. The etching was done by sprinkling zinc powder on the edge of the glass substrate and after that, the zinc was removed by using 30 vol% of hydrochloric acid (HCL). HTL, such the WO_3, WC and PEDOT:PSS were deposited/grown on the ITO. Then the active layer *a*-AlO_xN_y:Tb was deposited followed by the deposition of the ETL as the ZnO. The device was completed with Al electrodes.

Figure 4.2 shows a schematic structure of the DCTFEL devices including information of the thickness of each grown layer and also its bandgap diagram, where the theoretical work function value of each material is depicted. The green stripes represent the energy levels of the Tb^{+3} corresponding to the $^5D_4 \rightarrow {}^7F_j$ transitions.

HTL and ETL are chosen with the idea of reducing the large energy difference between the band offsets of the active layer and the electrodes. The HTLs bridge between the work function of the ITO and the energy in the minimum of the conduction band. ETLs bridge between the work function of the Al electrode and the energy at the maximum of the conduction band. The thicknesses of the HTLs and the ETLs were approx. 10 nm.

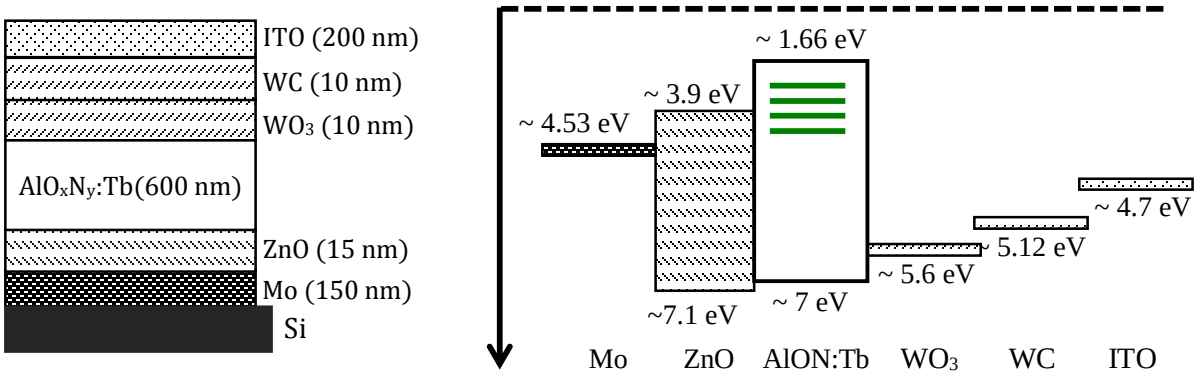

Figure 4.2 Schematic structure and band diagram of the DCTFEL device.

b) ACTFEL devices.

The fabrication of the inverted structure ACTFEL devices is comprising of the following layer on a SiO_2 (50 nm) that was grown on the silicon substrate by dry oxidation in order to prevent diffusion of impurities at the interface between the substrate/electrode when the samples are heated high temperatures. Molybdenum was used as the cathode electrode for all the devices. The insulating layers are grown on both sides of the active layer to prevent breakdown. Al_2O_3 and Si_3N_4 were used as insulator materials due their good dielectric properties. The ACTFEL devices were finalized by ITO or AZO as transparent electrodes. Figure 4.2 shows the schematic structure of the EL devices including information of the thickness of each grown layer.

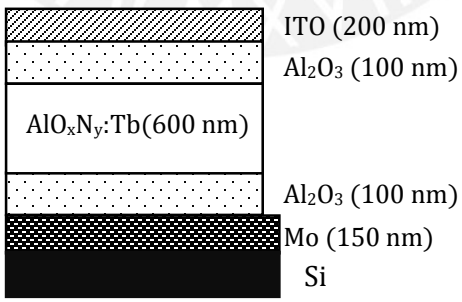

Figure 4.3 Schematic structure of the ACTFEL device.

In contrast to the DCTFEL devices, in this case, the work function of the layers in not a priority. Since the electrodes are used only for the application of the voltage and the insulating layers to protect the active layer from dielectric breakdown.

4.2 Characterization techniques

4.2.1 SEM and EDX measurements

Scanning electron microscopy images were taken on a Hitachi S 4800 using an acceleration voltage of 30 kV and sample current of approx. 11 µA in order to capture high resolutions images. Different magnifications of 10, 25, 50 and 100 kx were used to measure the grains with a suitable resolution. EDX spectra were obtained using a SEM Philips XL30 equipped with an EDAX system. All the EDX spectra were accumulated during 100 s with a spot size of 6.4, an acceleration voltage of 4 kV and a sample current of around 16 µA. The low acceleration voltage was chosen in order to not penetrate the substrate with the electron beam and, therefore, to avoid the silicon signal of the substrate.

4.2.2 XRD measurements

The diffraction experiments were performed on a Bruker D5000 theta-theta X-ray diffractometer equipped with a Cu Kα ($\lambda = 0.15418$ nm) radiation source and a Goebel mirror. Grazing incidence diffraction at 3° was performed to get higher intensity by the detector and avoid the substrate signal. X-ray experiments were carried out using a time/step of 1.3 s, a step-size of 0.02°/step. and a diffraction angles (2θ) covering the range from 20 to 100 °. The identification and of the layer analysis of the crystalline structure were done using the EVA software and the PDF file 048-0686.

4.2.3 FTIR measurements

Samples grown in silicon, where used for the infrared (IR) absorptions measurement, since silicon is transparent in the IR region. IR experiments were measured on carried out using an infrared spectroscopic ellipsometer SE 900 by SENTECH. The spectrometer SE 900 is equipped with a SiC source to generate the infrared light, a beam splitter, and a detector. During the measurements, the equipment was purged by N_2 to avoid the signal of water. The IR spectra are recorded in the wavenumber range from 200 to 4000 cm^{-1} with a resolution of 8 cm^{-1} and 512 scans. All the FTIR data were acquired with the SPECTRARAY II software in the transmittance mode.

4.2.4 XPS measurements

A SAGE HR 150 system equipped with an Ar sputter etching was used for the XPS measurements. The experiments were performed at a base pressure of 10^{-8} mbar. A mono-chromatic AlKα (1486.6 eV) radiation from an X-ray source operating at 300 W and 14 kV was use for the generation of photoelectrons in the surface region of the sample. The quantification and fitting of the XPS spectra were done using the software CasaXPS.

4.2.5 CL and PL measurements

The cathodoluminescence (CL) measurements were done in a Universal Evaporation Equipment. The CL spectra were measured at room temperature using an acceleration voltage of 30 kV and in the spectral range from 190 to 800 nm. The slit was set up to 100 µm giving a resolution of 0.45 nm at 546 nm. PL spectra were obtained by exciting the sample with a wavelength of 310 nm. The desired wavelength was obtained by collimating the light from a UV.VIS lamp with a monochromator. The emission spectra were recorded at the excitation wavelengths from 390 to 700 nm.

4.2.6 Experimental setup of the EL

The EL setup consists of a substrate holder attached to a microscope and two tips to contact the electrodes of the devices. The geometry of this set-up allows the measurements of devices with small electrodes with areas of the order of nanometers. A source meter Keithley 2410 is used to supply a constant current. The source is able to supply up to 250 V under a frequency of 1 kHz. Jobin Yvon Triax 320 monochromator is used to record the EL signal at room temperature.

4.2.7 Rapid thermal processing furnace (RTP)

The samples were heated using a Jipelec JetFirst RTP. The furnace consists of a halogen lamp to heating the sample, a purge gas line, and a cooling system. The samples were heated in a nitrogen atmosphere for six minutes. The RTP heating rate was 10 K/s and the cooling rate was 3 K/s.

5. Results and discussions

The following section is divided in two parts. First, the study of the morphological, vibrational, structural and luminescence properties of the terbium doped thin films and a comparison to the un-doped films in the as deposited state. The effect of the annealing temperature on the terbium doped layers also will be discussed. Second, the design and production of EL devices using as active materials the characterized films.

The characterization of the *a*-SiC_xO_y, *a*-AlO_xN_y, *a*-SiC_xO_y:Tb and *a*-AlO_xN_y:Tb thin films will be presented and discussed in the following sub-section. Different analytic techniques have been performed to study the effect of the Tb^{3+} in the amorphous SiC_xO_y and AlO_xN_y matrices. EDX was performed in order to investigate the stoichiometry of the films. The amorphous and crystalline states of the samples were confirmed by XRD measurements. FTIR was carried out to identify the vibrational bond states of the samples. However, the Tb^{3+} bonds are not easy to recognize in the FTIR spectra and also no references in the literature are reported until now. Therefore, XPS measures were performed in order to identify directly the bonding states of Tb^{3+} with other possible elements. Finally, light emission spectra were obtained under sub-bandgap photon excitation (PL) and band-to-band electron impact excitation (CL).

The effect of the annealing temperature is also discussed. The samples were heated at 500 °C, 750 °C and 1000 °C using an RTP furnace in a nitrogen atmosphere. Finally, first steps for the fabrication of the EL devices were proposed to be designed. Inverted and conventional ACTFEL and DCTFEL devices were fabricated. Photoluminescence measurements of the devices present good light emission spectra. Nevertheless, light emission spectra by EL measurements were not possible to obtain from the devices. However, possible reasons for why they could not work will be mentioned and further improvements in the design of the devices will be discussed.

5.1 SEM analysis

SEM images were performed in order to identify the surface morphology of the samples and also to measure the thickness. The layers were measured with a magnification of 100 kx in order to have detailed information of the surface morphology. The un-doped *a*-AlO_xN_y and doped *a*-AlO_xN_y:Tb layers were cleaned in an Ar sputter etching equipment during two minutes with the purpose of performing the XPS measurements, after that, the SEM images were carried out. Figure 5.1 (a), (b) and (c) show the SEM images before the sputter etching for the *a*-AlO_xN_y film and after the cleaning for the *a*-AlO_xN_y and *a*-AlO_xN_y:Tb layers. The surface morphology of the un-doped samples consists of clusters. The doped sample also presents morphology of clusters, but they are less pronounced that in the case of the un-doped layer.

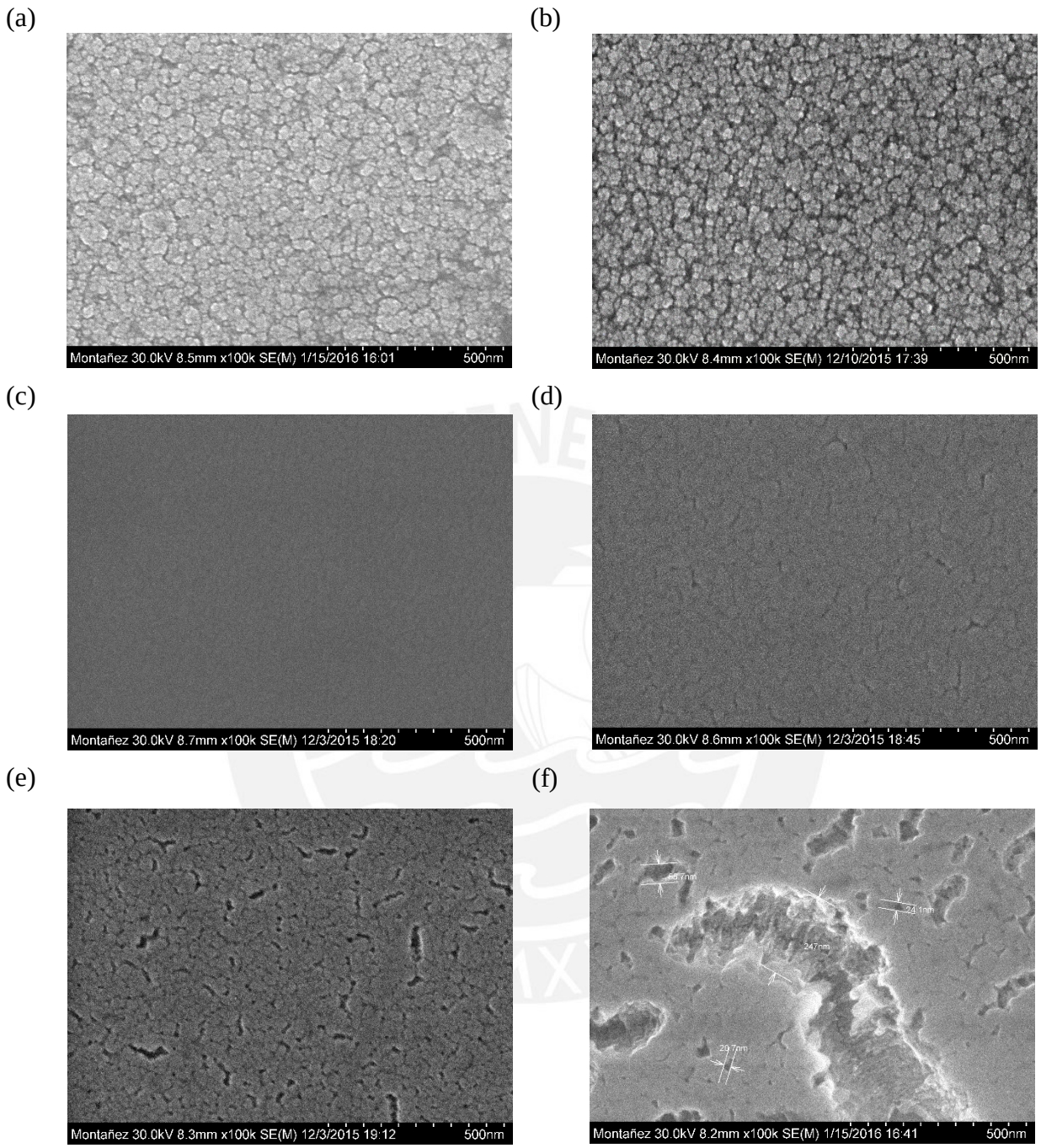

Figure 5.1 SEM images of the un-doped a-AlO_xN_y films without (a) and after sputtering etching(b). SEM images for the doped a-AlO_xN_y:Tb layer at room temperature (c), and for the samples heated at 500 °C (d), 750 °C (e) and 1000 °C (f) in an RTP furnace. The images were taken at 100 k of magnification.

Figure 5.1 (d to f) show SEM images for the *a*-AlO_xN_y:Tb layers, the samples were previously heated in an RTP furnace at temperatures of 500 °C, 750 °C and 1000 °C. The surface morphology at different annealing temperatures reveals a grainy and fractured appearance. The

size of the fractured region increases as the annealing temperature increases. The fracturing of the layers might be attributed to the difference of the thermal expansion coefficient of the substrate and the film and also due residual stress.

Figure 5.2 (a) and (b) show the SEM images for the un-doped *a*-SiC_xO_y layers, which consist of clusters with different dimensions ranging from 16 nm to 24 nm. Figure 5.2 (c) and (d) show the SEM images of the *a*-SiC_xO_y:Tb layers at room temperature and after an annealing temperature at 1000 °C. At room temperature, the surface of the doped layer is nearly flat. At 1000 °C tiny grains are observed. Nevertheless, they are not well defined due the charging effect during the measurements. No fracture appearance is observed like in the case of the *a*-AlO_xN_y:Tb layers.

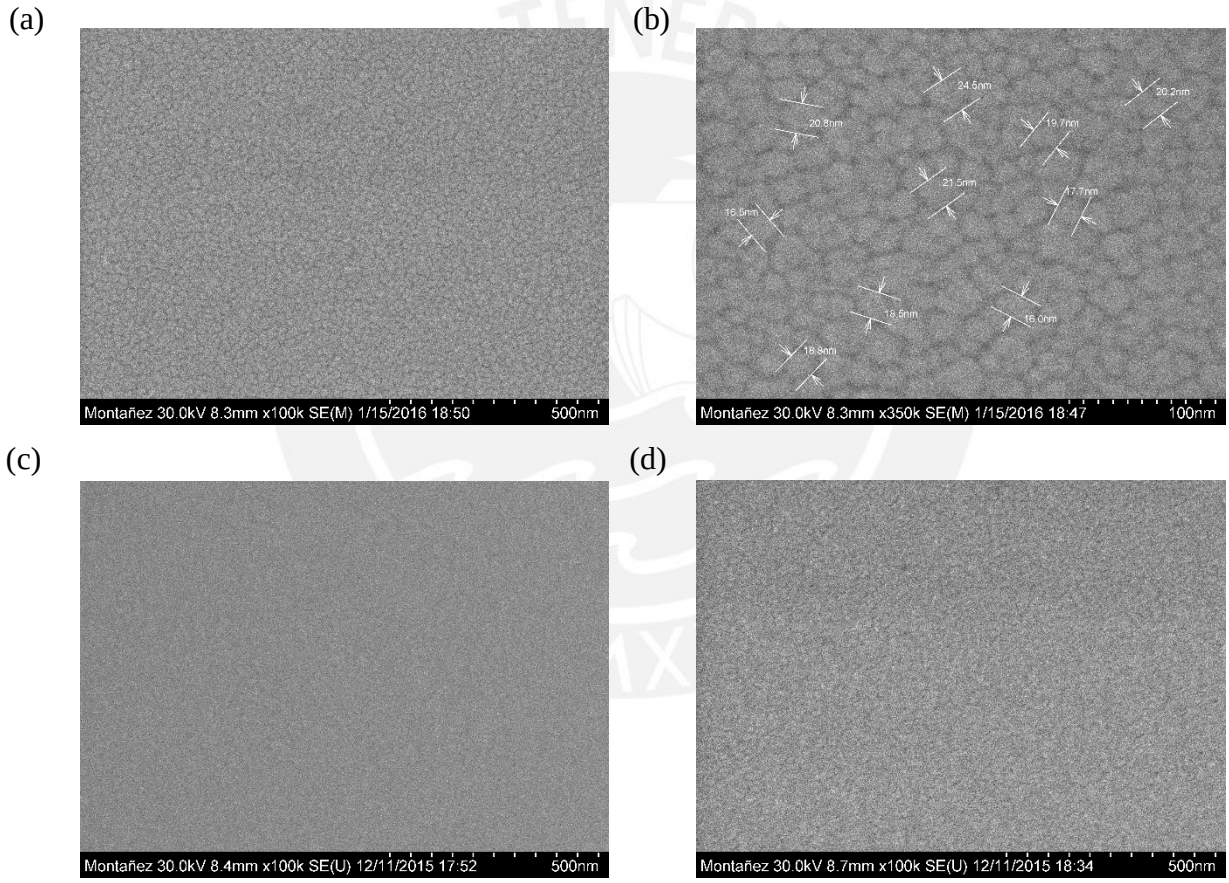

Figure 5.2 SEM of the un-doped a-SiC_xO_y (a) and (b) and doped a-SiC_xO_y:Tb layer at room temperature (c) and heated at 1000 °C in an RTP furnace before the measurement(d).

In order to measure the thickness, the samples were fixed in the substrate-holder with an angle at 90 ° in reference to the electron beam source. Figure 5.3 shows the thickness of the un-doped *a*-AlO_xN_y and *a*-SiC_xO_y and doped *a*-AlO_xN_y:Tb layers. The thicknesses of the AlO_xN_y:Tb are in the range from 246 nm to 375 nm and in the case of the *a*-SiC_xO_y is 137 nm.

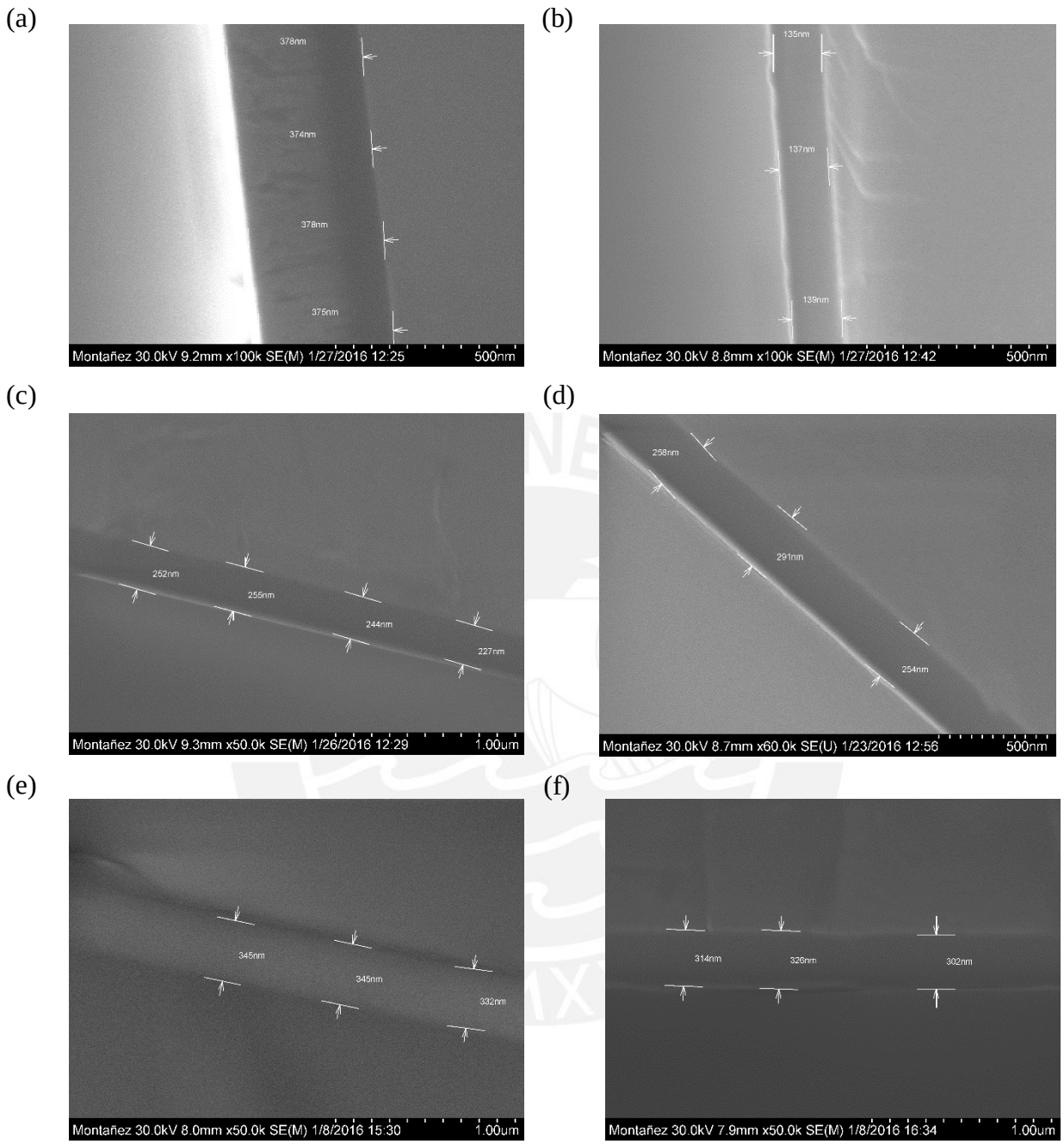

Figure 5.3 SEM images of the un-doped a-AlO_xN_y (a), a-SiC_xO_y (b) and doped a-AlO_xN_y:Tb (c) layers at room temperature. a-AlO_xN_y:Tb sample were heated before the measurements at 500 °C (d), 750 °C (e) and 1000 °C (f).

5.2 EDX analysis

Figure 5.4 shows the typical EDX spectra for the undoped *a*- SiC_xO_y and *a*-AlO_xN_y and doped *a*- SiC_xO_y:Tb and *a*-AlO_xN_y:Tb thin films in the as-deposited state. *a*-AlO_xN_y and *a*-AlO_xN_y:Tb thin films are composed of aluminum, nitrogen and oxygen. A small amount of carbon was also found as impurity due to the absorbents in the atmosphere (Figure 5.4 (a-b)). The average Al/N

ratio was 1:0.59 and 1:0.57 for the un-doped and doped layers, respectively, indicating a low incorporation of nitrogen. The un-doped layer exhibited no signal in the region of the terbium, whereas the doped layer shows the characteristic signal of terbium, confirming the incorporation of it in the amorphous matrix.

The EDX spectra of *a*- SiC_xO_y and *a*- SiC_xO_y:Tb layers show the presence of carbon, oxygen, and silicon (Figure 5.4 c,d). The doped film presents an extra peak corresponding to the terbium. A precise quantification of the elements of these two layers was not possible, since the signal of carbon is a contribution of the layer and impurities and the signal of silicon and oxygen might be a contribution of the layer and the substrate. Nevertheless, EDX is useful in order to confirm the terbium in the doped layer.

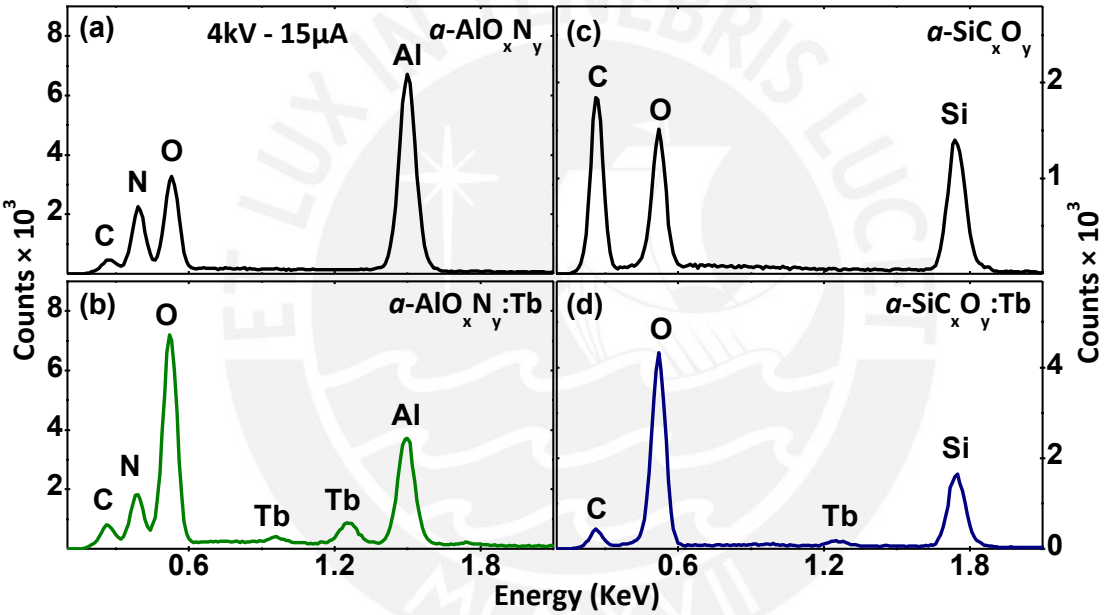

Figure 5.4 EDX spectra showing the elemental composition of the a-AlO_xN_y (a), a-AlO_xN_y:Tb (b), a-SiC_xO_y (c) and a-SiC_xO_y:Tb (d) thin films.

Since the substrate holder of the sputtering system used for the growth of the active layers is fixed and due the flexible geometry of the magnetrons, the terbium concentration changes throughout the layer. Therefore, EDX measurements were carried out in different positions of two pieces of *a*- AlO_xN_y:Tb layers collocated in different places of the substrate holder. The terbium power for that process was 15 W. The size of the sample is around 40 mm×15 mm. EDX spectra were measured every 2.5 mm.

Figure 5.5 shows the variation of the terbium in at. % as a function of the distance. When the sample has a parallel orientation between the AlN and Tb targets, the Tb concentration decreases from 1.19 to 0.31at. % in 40 mm (Figure 5.5 a). In the case, of the sample has a perpendicular

orientation, the Tb concentration is oscillating between 2.7 and 3.7 at.% (Figure 5.5 b). The advantage of the geometry of the flexible magnetrons is the possibility to reach different Tb concentration in one process.

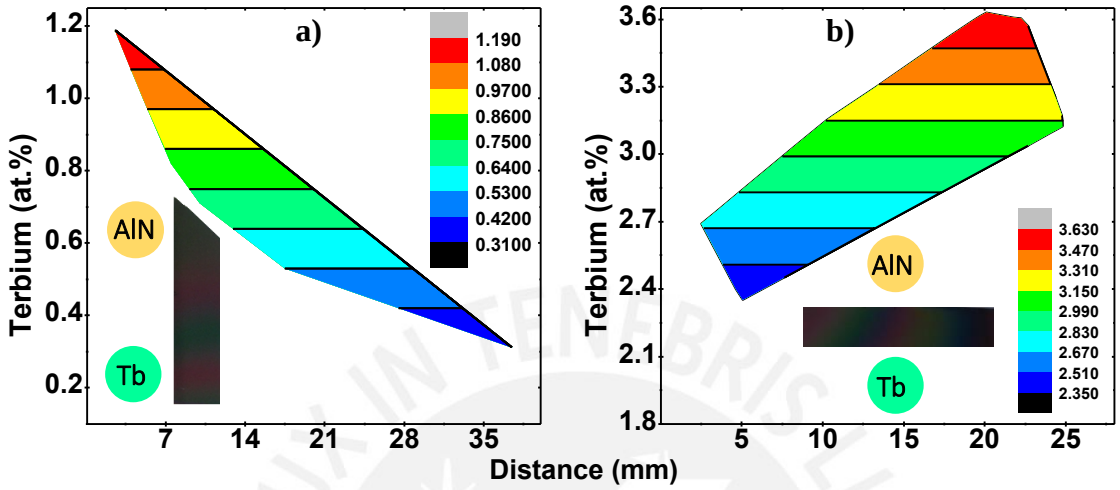

Figure 5.5 EDX spectra showing the terbium concentration (at. %) of the a-AlO_xN_y:Tb thin films as a function of the distance. The Tb was measured every 2.5 mm. The circles show the position of the AlN and Tb targets.

It was demonstrated, that the highest light emission intensity of Tb occurs for concentration around 1 at.% [13]. Therefore, the samples were cut into small pieces (around 5 mm×8 mm), then all samples with terbium concentration of around 1 at.% were heated at annealing temperatures of 500 °C, 750 °C and 1000 °C. The percentage atomic concentration analysis of the elements in the film has been calculated and the constituent elements are shown in Table 5.1. As the annealing temperature increases, the atomic concentration ratio between the Al/Tb is nearly constant. Except, with the sample heated at 750 °C.

Table 5.1 Elemental composition for the undoped a- AlO_xN_y and terbium doped a- AlO_xN_y:Tb thin films at room temperature (RT) and at annealing temperatures of 500 °C, 750 °C and 1000 °C. The Al/Tb and their respective errors (d(Al/Tb)) are also included.

	C (at. %)	N (at. %)	O (at. %)	Tb (at. %)	Al (at. %)	Al/Tb	d(Al/Tb)
RT (*a*-AlO_xN_y)	7.86	26.54	20.37	-	45.23		
RT (*a*-AlO_xN_y:Tb)	8.51	9.80	47.12	1.23	33.34	27.11	7.74
500 °C	9.36	15.85	44.39	1.29	29.1	22.56	6.32
750 °C	9.00	7.86	46.43	0.93	35.78	38.47	11.00
1000 °C	10.72	7.49	43.09	1.49	37.22	24.98	7.10

5.3 XRD analysis

Investigation of the structure of the active layers grown on silicon substrates was performed by XRD at grazing incidence of 3 °. Figure 5.6 (a) shows the arrangement of the silicon substrates in one deposition process. The rectangles represent the silicon substrates and the circles represent the AlN and Tb targets. XRD patterns of the layer in position 1 (process A) are mostly amorphous, except for one measure (Figure 5.6 b, process A). In the case of process X, samples in position 2 are crystalline, whereas samples in position 4 and 5 are amorphous. XRD patterns reveal an amorphous state with partial crystalline areas. It could happen due the non-uniform cooling of the substrate during the deposition process.

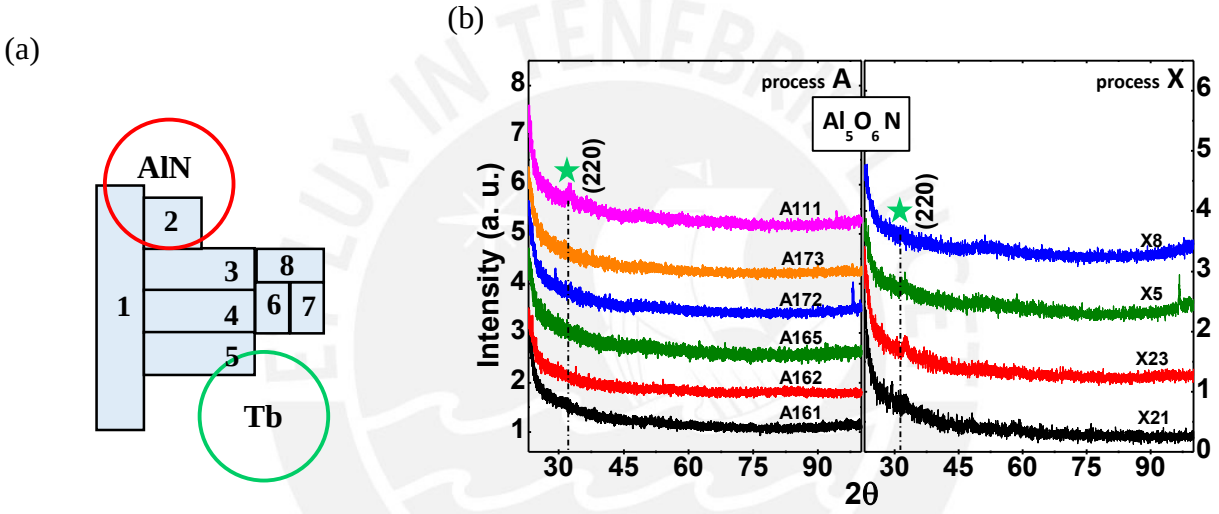

Figure 5.6 Arrangement of the silicon substrates on the holder substrate (rectangles) and AlN and Tb targets (circles) (a). XRD patterns of sample A on position 1 and sample B in positions 2, 5 and 8 correspondent to the AlO_xN_y:Tb thin films in the as deposited state.

The crystalline peak appeared at the diffraction angle of 32.32 ° has low intensity. However, it could be assign to the hexagonal aluminium oxynitride (Al_5O_6N) structure. Therefore, the peak at 32.32 ° correspond to the (220) crystalline plane. The FWHM of this peak is 1.5 and the calculated grain size is 5.5 nm. The existence of the small crystalline regions was another motivation to cut the samples in small areas. XRD was taken from all the small pieces in the as deposited state in order to choose samples in amorphous state with terbium concentration of around 1 at.%, after that, the samples were heated in the RTP furnace.

Figure 5.7 shows a series of XRD diffractograms for the un-doped and doped *a*- SiC_xO_y:Tb as well as *a* -AlO_xN_y:Tb samples at room temperature and after annealing temperatures at 500 °C and 750 °C and 1000 °C. XRD patterns for the un-doped (Ref) and doped *a*- SiC_xO_y:Tb revealed an amorphous nature.

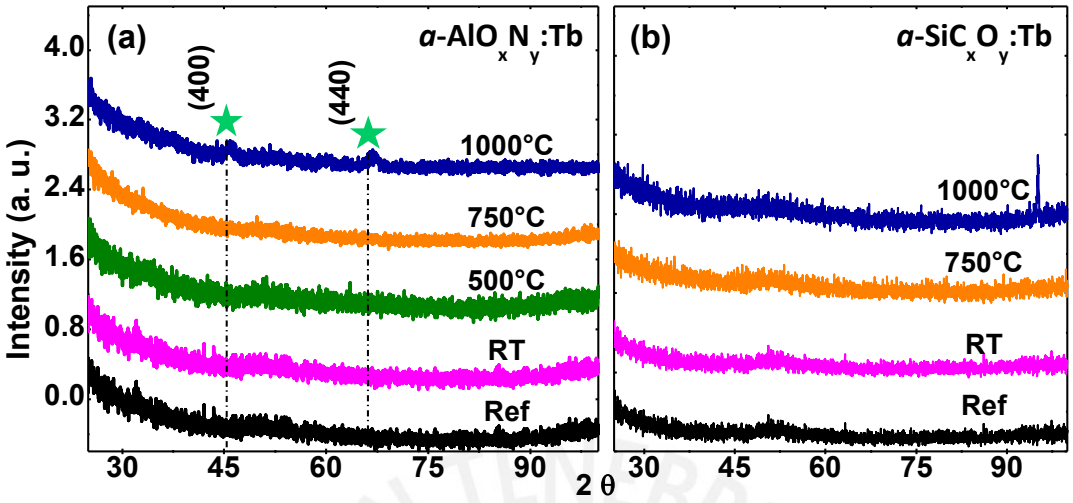

Figure 5.7 GIXRD diffraction patterns of the un-doped (Ref) and doped a-AlO_xN_y:Tb (a) as well as a- SiC_xO_y:Tb (b) thin films at room temperature and after a heating in an RTP furnace at 500 °C, 750 °C and 1000 °C.

XRD patters of the a-AlO_xN_y:Tb reveal clearly an amorphous nature at room temperature and for samples heated at 500 °C and 750 °C in a RTP furnace. In contrast, after an annealing at 1000 °C the XRD pattern shows two crystalline peaks. According to the PDF file 048-0686, the film has a cubic structure corresponding to the Al_5O_6N. The two peaks at the 2θ values of 45.83 ° and 66.83 ° can be assigned to the (400) and (440) crystallographic orientations, respectively. The FWHM of the (400) and (440) crystallites were 0.83 ° and 0.85 °and the calculated average grain size according to the Scherrer equation were 10.4 nm and 11.2 nm, respectively. A shift of the crystalline peaks is observed; it can occur due residual stress as is observed in the SEM imagines. In the case of the *a*- SiC_xO_y:Tb, the sample remains amorphous until 1000 °C.

5.3 FTIR analysis

The characteristic infrared absorption spectra after baseline subtraction and thickness normalization of the undoped *a*-AlO_xN_y and terbium doped *a*- AlO_xN_y:Tb thin films are shown in Figure 5.8. The identification of the vibrational modes was taken from different references [66–68]. FTIR measurements reveal the formation of Al-N and Al-O vibrational modes.

The main vibration modes occur within the spectral range from 400 cm^{-1} to 1100 cm^{-1} which were magnified and shown in the inserted graphics in order to show the active modes better. Due the amorphous nature of the sample, the fittings of the vibrational modes are well suited with Gaussians. The broad absorption band is the overlap of three vibration modes corresponding to Al-O, Al-N and Al-O-Al modes at 561 cm^{-1}, 654 cm^{-1} and 764 cm^{-1}, respectively. The broad band from 2900 cm^{-1} to 3800 cm^{-1} is due the H-O vibrations modes.

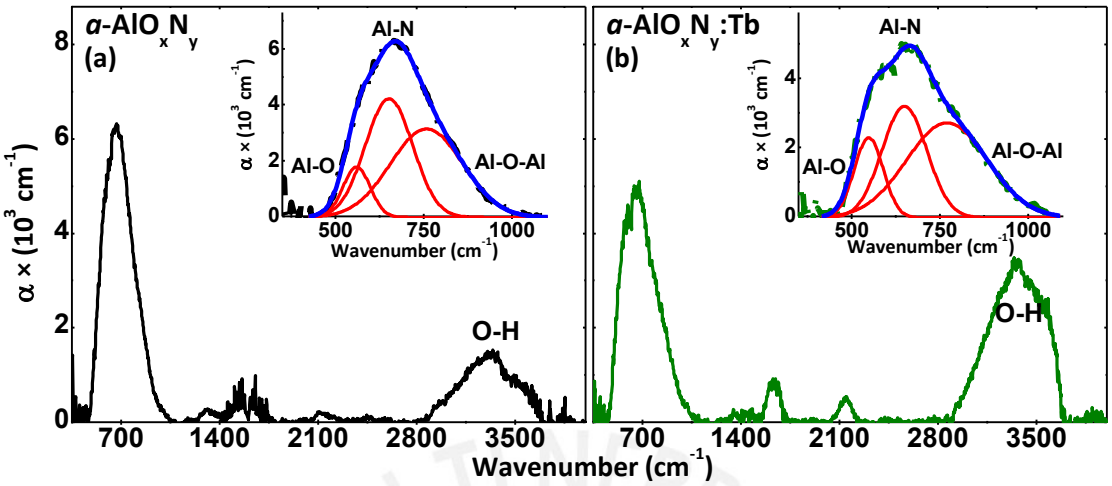

Figure 5.8 FTIR absorption spectra of the a-AlO_xN_y (a) and a-AlO_xN_y:Tb (b) thin films deposited on silicon substrates.

There are no additional vibration peaks for the doped film. However, the difference between the doped and un-doped films is in the intensity ratio of the broad bands around 700 cm^{-1} and 3400 cm^{-1} which is 1:0.28. The terbium is usually bonded to oxygen atoms, therefore, the incorporation of terbium in the host matrix induce the formation of higher Al-O and O-H vibrational modes than the un-doped sample.

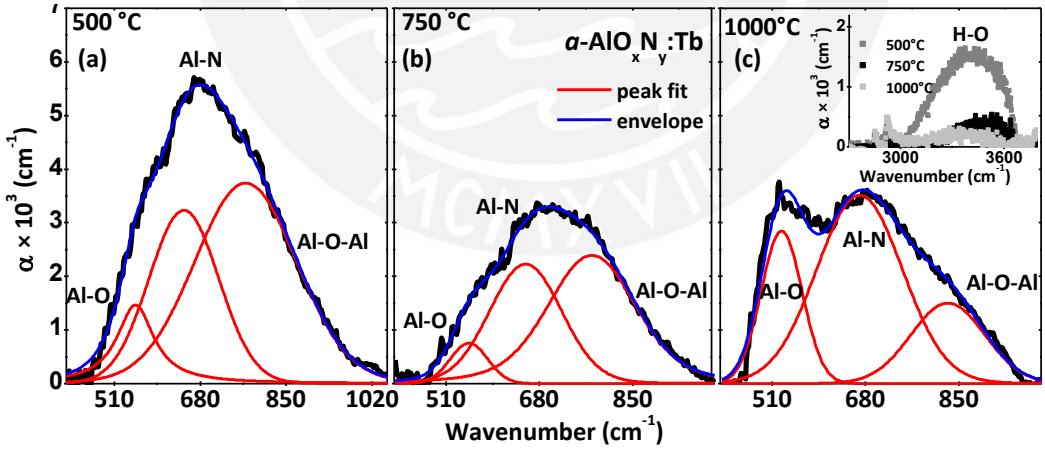

Figure 5.9 FTIR absorption spectra of the a- AlO_xN_y:Tb thin films deposited on silicon substrate. The samples were heated before the measurements using a RTP furnace at 500 °C (a), 750 °C (b) and 1000 °C (c). Inset graphics shows the decrease of the H-O vibrational modes.

FTIR absorption spectra of the *a*- AlO_xN_y:Tb thin films after annealing temperatures at 500 °C, 750 °C and 1000 °C are shown in Figure 5.9. The intensity of the Al-N bonds decrease with the annealing temperature until 750 °C, whereas Al-O-Al peaks increase. At the same time, H-O

bonds decrease with the annealing temperature. However, at 1000 C the FTIR spetrum shows a strong change, in which the Al-O peak increases and becomes narrow due the crystallization process, which was revealed by the XRD measurements. Crystallization induces the reorganization of the atoms and, therefore, the average of the bound length of the Al-O bonds becomes closer. In this case, the Al-O a 1000 °C was fitted using a Lorentzian function.

FTIR spectra of the *a*-SiC_xO_y and *a*-SiC_xO_y:Tb confirm the formation of Si-O and Si-C bonds of the samples (Figure 5.10). The identification of the vibrational modes was taken from different references [69–72]. The FTIR spectrum of the un-doped *a*-SiC_xO_y film presents two visible bands of interest (Figure 5.10a). The band at around 780 cm^{-1} corresponds to the Si-C stretching mode, and the strong shoulder can be attributed to the overlapping of four bands associated to Si-O stretching bonds from which it is possible to distinguish an average at 1047 cm^{-1} [69][73]. Another Si-O stretching related vibrational mode can also be observed at 416 cm^{-1} as a small peak compared to the latter ones.

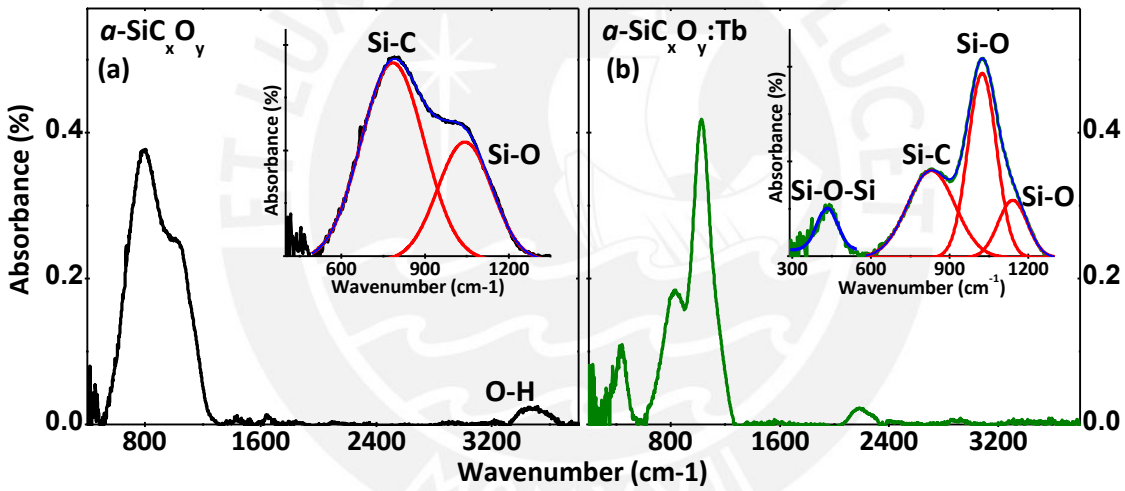

Figure 5.10 FTIR absorption spectra of the a- SiC_xO_y (a) and a- SiC_xO_y:Tb (b) thin films deposited on silicon substrates. The broad band is zoomed and shown in the insert graphics to appreciate the characteristic vibrational bonds.

The FTIR spectrum of the *a*-SiC_xO_y:Tb film is shown in Figure 5.10 (b). The main absorption band is observed in the region from 600 cm^{-1} to 1250 cm^{-1}. The bands are associated with the Si-C, Si-O and Si-O at 827 cm^{-1}, 1024 cm^{-1} and 1142 cm^{-1}, respectively. Other Si-O peak is observed at 439 cm^{-1} and the peak at 2180 cm^{-1} can be attributed to the Si-H bond.

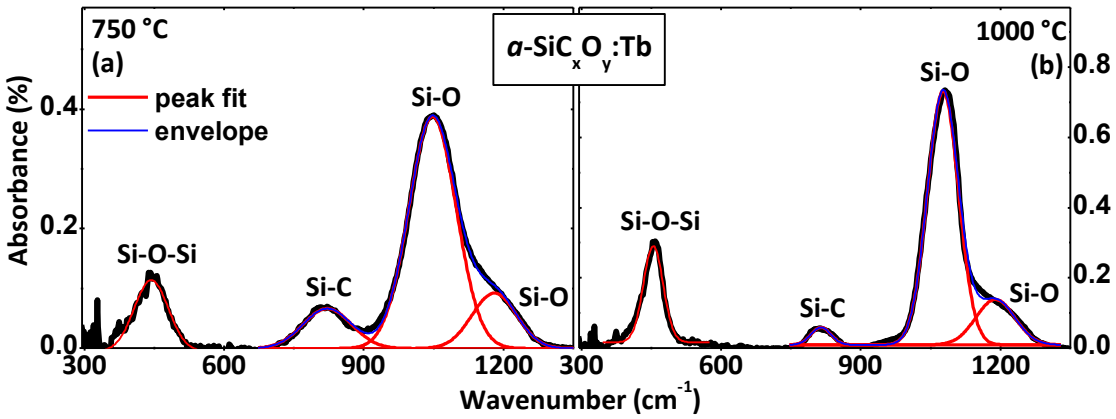

Figure 5.11 FTIR absorption spectra of the a- SiC_xO_y:Tb thin films. The samples were heated before at temperatures of 750 °C (a) and 1000 °C (b) in a RTP furnace.

Figure 5.11 shows the fit of the FTIR spectra of the *a*- SiC_xO_y:Tb layer after their heating in a RTP furnace at 750 °C and 1000 °C. The positions of all the described modes are observed with slight changes in the wavenumbers at different annealing temperatures in both cases. The position of the peaks changed according to the arrangement of the atoms in the matrix. The Si-C mode decreases with the annealing temperature, while Si-O bonds are enhanced and the FWHM becomes narrow. At 1000 °C a weak Si-C bond is observed. At this point, the stoichiometry of the sample is close to the silicon oxide.

5.4 XPS analysis

A first XPS spectrum of the *a*-AlO_xN_y film revealed contamination by carbon species, due absorbents in the atmosphere. Therefore, the surface of the films was sputtered under an Ar atmosphere for two minutes. After the sputter etching the strong carbon signal almost disappeared (see Figure 5.12). Typical XPS spectra before and after the sputter for the un-doped *a*-AlO_xN_y films are depicted in Figure 5.12. The XPS spectrum of the doped *a*-AlO_xN_y:Tb are also included.

The binding bonds were identified by comparison with different references [63–65]. Un-doped and doped samples present the Al2s, Al2p, N1s, O1s and C1s lines. The *a*- AlO_xN_y:Tb thin film shows two extra lines corresponding to Tb4d and Tb3d. MNN and KLL Auger lines appear at around 600 eV and 990 eV, respectively. Ar2p line also appears as a result of the sputtering.

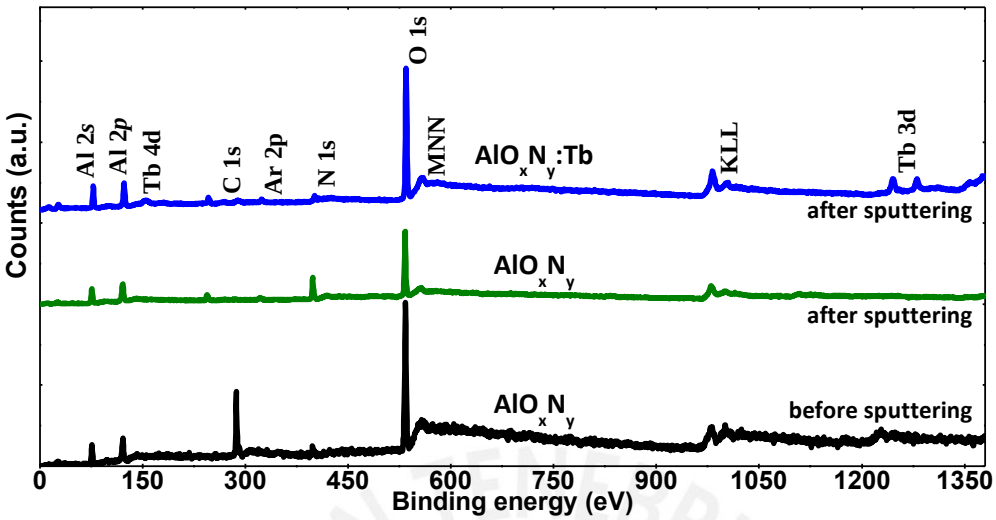

Figure 5.12 XPS spectra of the un-doped a-AlO_xN_y layer before and after the sputter etching and for the doped a-AlO_xN_y:Tb thin film showing the characteristics photoelectron lines of Al2s, Al2p, N1s, O1s, C1s, Tb4d and Tb3d. The intensity of the C1s core level becomes weak after the sputter etching. Auger lines MNN and KLL also appeared. Due the sputtering of the surface of the samples the Ar2p line appears.

In order to evaluate each core level, high resolution spectra scan of the Al2p, O1s, N1s and Tb3d were performed. Analysis and evaluation of the core levels were done with the CasaXPS software. All the core levels present a shift of around 3 eV in the binding energy axes due the charging effects during the measurements. Thus, all binding energies should be referenced with one core level. Since, the stoichiometry of Al, O, N and Tb elements are the desired ones, these core level cannot be used for calibration purposes. Therefore, all binding energies were referenced to the C1s peak at 385.6eV. Figure 5.13 shows the peak deconvolution of the Al2p, O1s, Tb3d and N1s. stoichiometry of Al, O, N and Tb.

In the case of the Al2p region, at room temperature, 500 °C and 750 °C the Al-O bonding is observed at around 74 eV, whereas at 1000 °C the Al-N appears at 72.6 eV (Figure 5.13 a). In the as deposited state, O1s core level is decomposed in two peaks at binding energies at 531.25 eV and 533.02 eV correspondents to the Al-O as the main bonding and the Al-OH. As the temperature increases the Al-OH peaks decreases and at 1000 °C, Al-O at a binding energy of 534.02 eV appears instead the Al-OH peak. Furthermore, at an annealing temperature of 1000 °C Tb_2O_3 appears at 529.4 eV (see Figure 5.13 b).

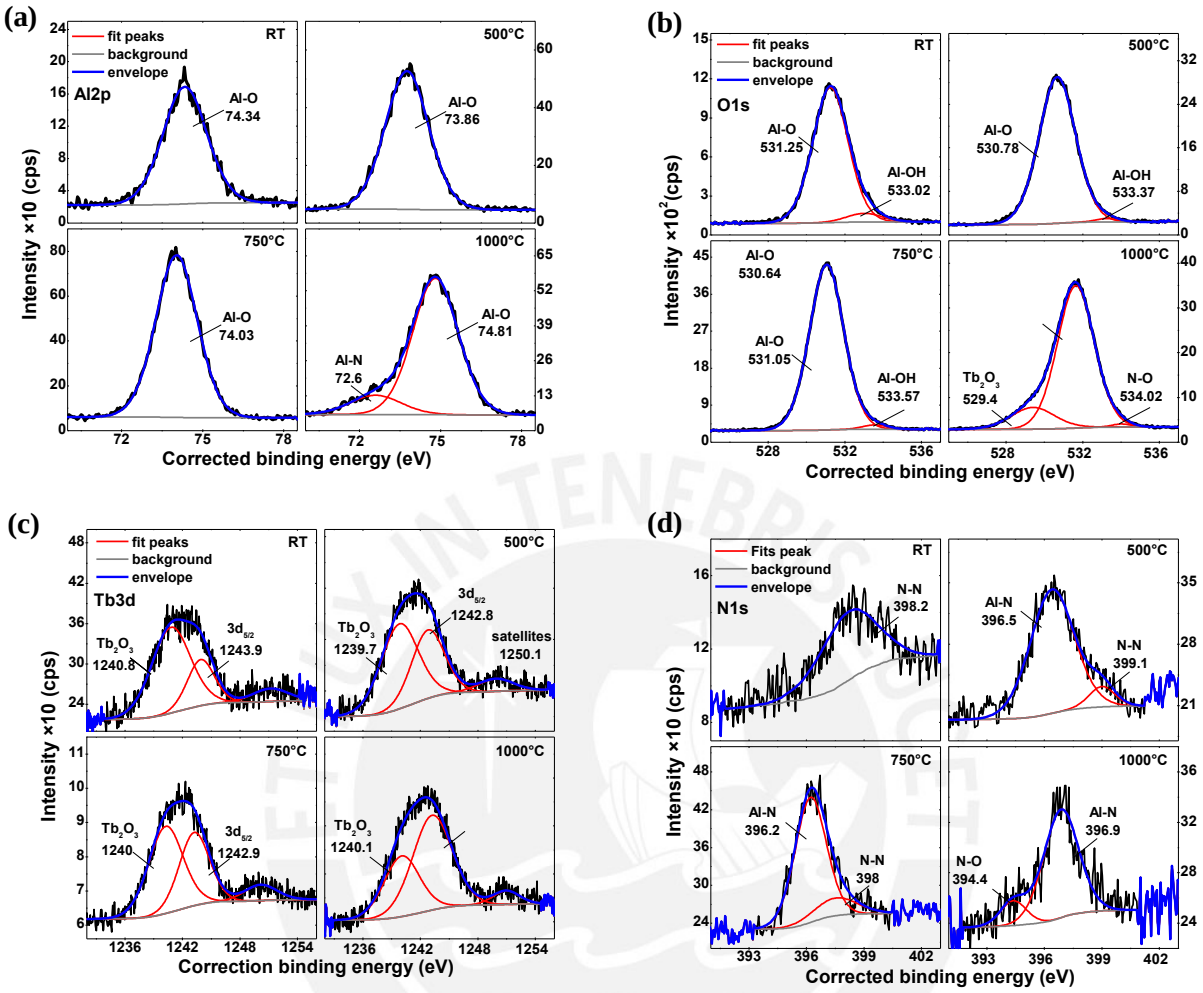

Figure 5.13 Peak deconvolution of the Al2p (a), O1s (b), Tb3d (c) and N1s (d), the samples were heated before in an RTP furnace at 500 °C, 750 °C and 1000 °C.

Figure 5.13 (c) shows the peak fits of the N1s core level, which consist of N-N bonds at a binding energy of 598.2 eV at room temperature. When the annealing temperature increases, the Al-N bond appears at 396.5 °eV. At 1000 °C, N-O bond is formed instead N-N bonds. Tb3d region consists of two peaks: Tb3d5/2 and Tb2d3/2 at around 1245 and 1280 eV, respectively. Figure 5.13 (d) shows the fitting of the Tb2d3/2, which presents the Tb_2O_3 peak at 1240.8 eV and also a week signal at 1250.1 eV due the satellites [74]. As the annealing temperature increases, the area of the Tb_2O_3 peak decreases. At 1000 °C the decrease in the area of Tb_2O_3 is strong. However, a new Tb_2O_3 at a binding energy of 529.4 eV is observed.

Depth profile of the *a*- AlO_xN_y:Tb layer heated at 750 °C was performed in order to know the elemental composition of the whole sample. Results show a slight change of the terbium

concentration, but only for the 6 first cycles, after that, the composition with depth is almost constant, although the flexible geometry of the magnetrons, from which a gradient variation of the composition could be expected.

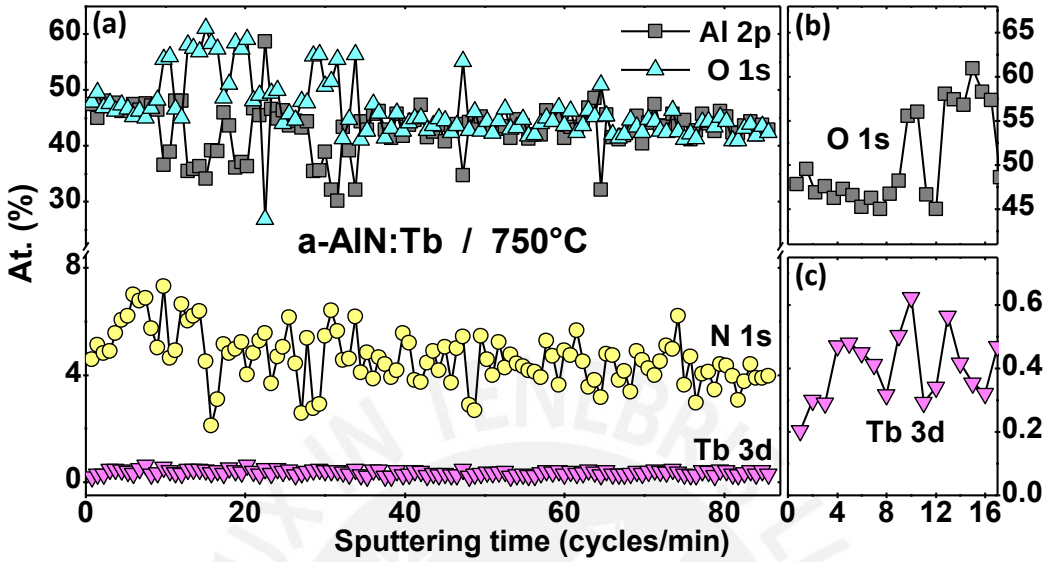

Figure 5.14 Depth profile of the a- AlO_xN_y:Tb layer after a heating at 750 °C in a RTP furnace.

Table 5.2 shows the surface elemental composition in atomic percent of the *a*- AlO_xN_y:Tb at room temperature and a heating temperatures of 500 °C, 750 °C and 1000 °C. The elemental composition of the XPS differs from the EDX results. In the case of the EDX, the measurements are in the whole film, while in the case of the XPS is at the surface. In the depth profile for the first 6 cycles the terbium concentration is also low (around 0.2) and, therefore, it slightly increases until 0.6. The small concentration of terbium with the annealing temperature can be also due diffusion of Tb through the cracks, which dimension increases with the annealing temperature (Figure 5.1 d-f).

Table 5.2 Elemental composition for the doped a-AlO_xN_y:Tb thin film layers at room temperature and at annealing temperatures of 500 °C, 750 °C and 1000 °C.

	C (at. %)	N_2 (at. %)	O_2 (at. %)	Al (at. %)	Tb (at. %)	Al/ Tb	O_2/ N_2
RT (*a*-AlO_xN_y)	3.09	17.21	29.47	50.23	-	1.71	1.71
RT (*a*-AlO_xN_y:Tb)	5.63	4.90	54.20	34.50	0.77	44.80	11.07
500 °C	7.11	5.37	48.03	38.86	0.63	61.46	8.94
750 °C	6.89	4.18	44.26	44.47	0.21	207.76	10.6
1000 °C	9.70	2.08	46.25	41.73	0.24	172.83	22.27

Figure 5.15 shows a comparison between the area of the Al-O and Al-N vibrational modes retrieved from the FTIR spectra and the area of the Al-O and Al-N binding energies retrieved from the Al2p and O1s core levels of the XPS. The Al-O binding energy of the Al2p core level remains almost constant until 750 °C while the Al-O from the O1s increases up to 500 °C and then decreases. However, since the Al2p core level has the higher intensity and, therefore, its behavior is the dominant one. The area of the Al-O vibrational modes shows a slight increase up to 500 °C and then it decreases. The behavior of the area of the Al-O vibrational bonds and the Al-O binding from the XPS as a function of annealing temperature is correlated.

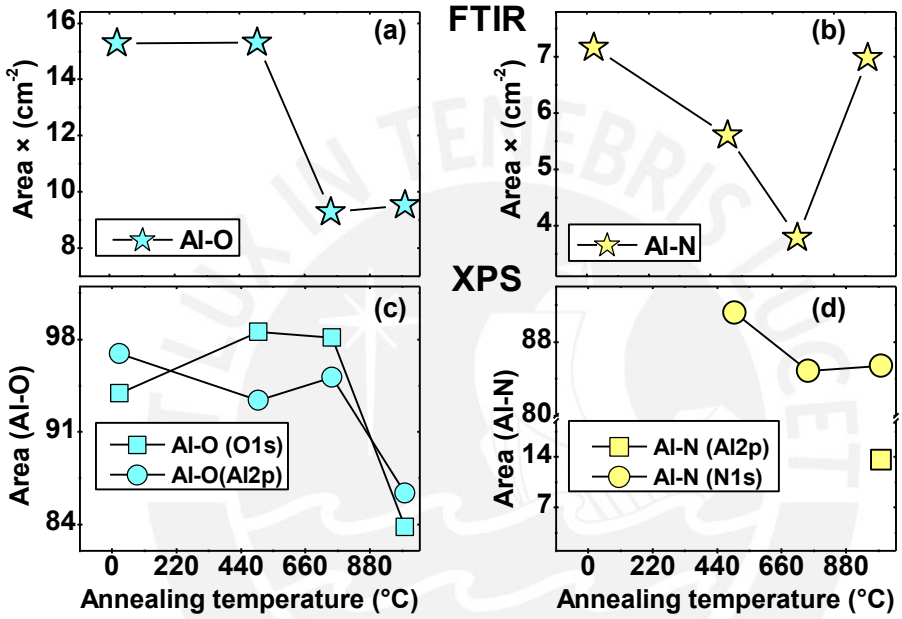

Figure 5.15 Comparison of the vibrational modes from the FTIR (a and b) and the binding energies from the XPS (c and d) of the a- AlO_xN_y:Tb layer at differentness annealing temperatures.

The area of the Al-N binding energy of the Al2p core level appears only at 1000 °C while the Al-N from the N1s core level appears at 500 °C and then decreases. In the case of the area of the Al-N vibrational modes, it decreases with the annealing temperature until 750 °C and then it increases at 1000 °C.

5.5 Light emission analysis

Light emission properties were performed on the active layers deposited on silicon substrates and, on the whole, devices. Light emission of the un-doped and doped *a*- AlO_xN_y:Tb and *a*- SiC_xO_y:Tb layers were performed by PL and CL. However, there was no light emission of terbium in the case of the *a*- SiC_xO_y:Tb layers.

The devices manufactured using *a*- AlO_xN_y:Tb as active layer were tested first by PL in order to make sure that the HTL and ETL do not opaque the emission of light through the active layer, then current/voltage (I-V) curves were done and finally EL measurements were performed.

5.5.1 CL, PLE and PL measurements on the active layers grown directly on Si substrates

The requirement for the CL measurements at the TU-Ilmenau is the dimension of the substrate. It should be high than 1 cm × 1 cm. However, the sizes for the *a*- AlO_xN_y:Tb layer were around 0.8 cm × 0.5 cm, therefore, only one sample was measured. The sizes of the *a*- SiC_xO_y:Tb (2 cm×2 cm) layers were suitable for the CL.

Figure 5.16 (a) shows the CL spectra for the *a*- AlO_xN_y:Tb layer in the as deposited state measured with an acceleration voltage of 30 kV (1.7 A) and for the sample heated at 700 °C in an RTP furnace (30 kV / 1.7 A). Both samples present the four characteristic $^5D_4 \rightarrow {}^7F_j$ transitions. Light emission of the heated sample at 700 °C decreases. Extinction of light emission intensity is known as concentration quenching.

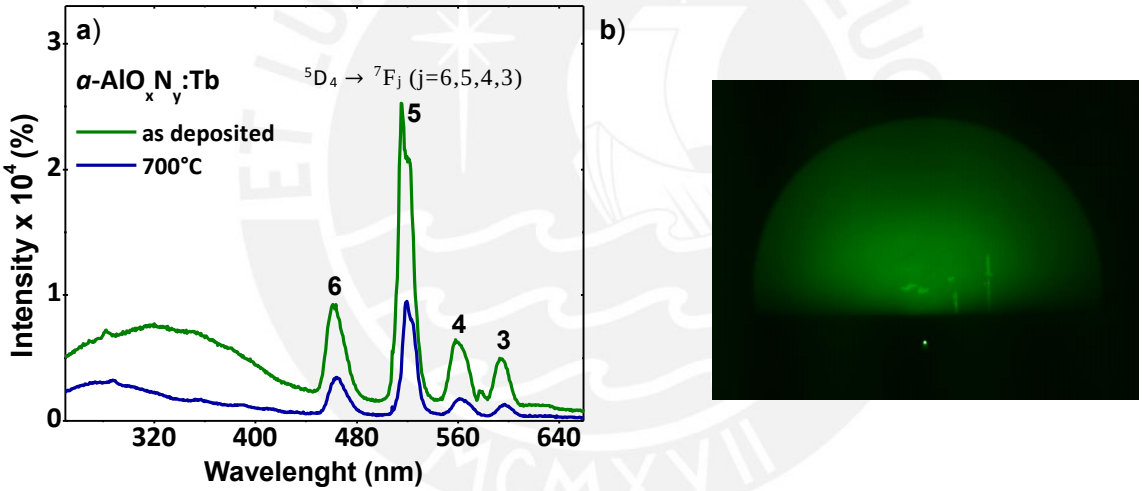

Figure 5.16 CL measurements for the a- AlO_xN_y:Tb layer in the as deposited state and heated at 700 °C in an RTP furnace (a). RHEED pattern for the heated sample(b).

Figure 5.16 (b) shows the reflection high-energy electron diffraction (RHEED) image of the heated sample, which shows a diffuse pattern indicating an amorphous surface structure. This fact is in good accordance with the XRD results, where no crystalline phase is found.

Photoluminescence excitation measurements (PLE) were performed before the PL in order to select the best wavelength excitation (see Figure 5.17 a). For the PLE measurements, the monochromator was fixed at 550 nm ($^5D_4 \rightarrow {}^7F_5$), the strongest emission line of Tb^{3+} and the spectrum was recorded in the range from 240 to 500 nm. The best excitation wavelength for the case of *a*-AlO_xN_y:Tb is 310 nm. Figure 5.17 (b) shows the room temperature PL emission for the

a-AlO_xN_y:Tb doped with 1.34 at. % Tb film. The spectrum shows the characteristic $^5D_4 \rightarrow ^7F_j$ transitions with emission peaks at about 502 nm, 558 nm, 600 nm and 634 nm.

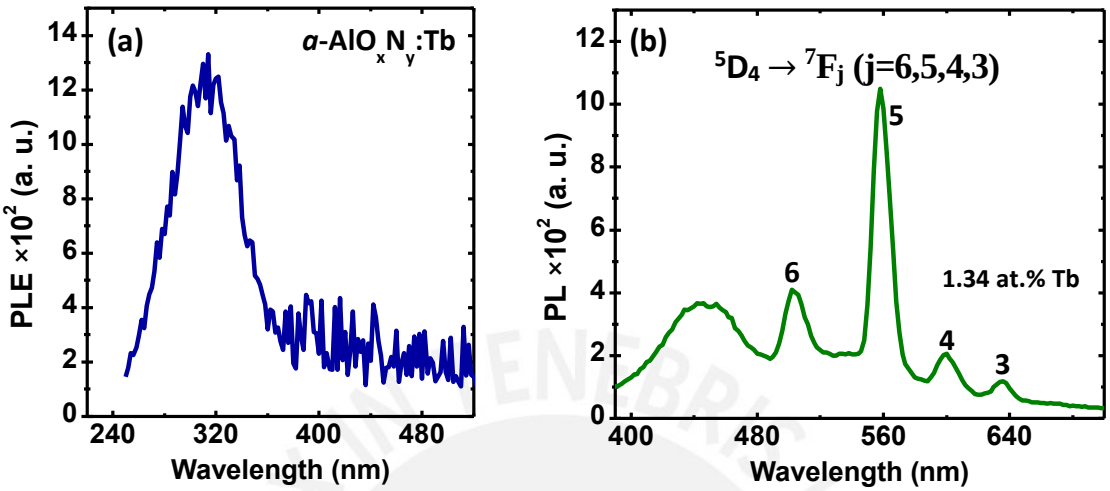

Figure 5.17 PLE (a) and PL (b) spectra of the doped a- AlO_xN_y:Tb thin film.

Figure 5.18 shows the integrated intensity of the $^5D_4 \rightarrow ^7F_5$ transition for terbium concentration from 0.4 up to 4.8 at.%. Two regions are clearly observed: Activation of Tb^{3+} emission and concentration quenching. In the activation region, as soon as more terbium ions are incorporated in the amorphous matrix, light intensity of the layers increases up-to around 1.3 at.%. After this concentration, when more terbium atoms are incorporated, light intensity starts to decrease slightly (concentration quenching).

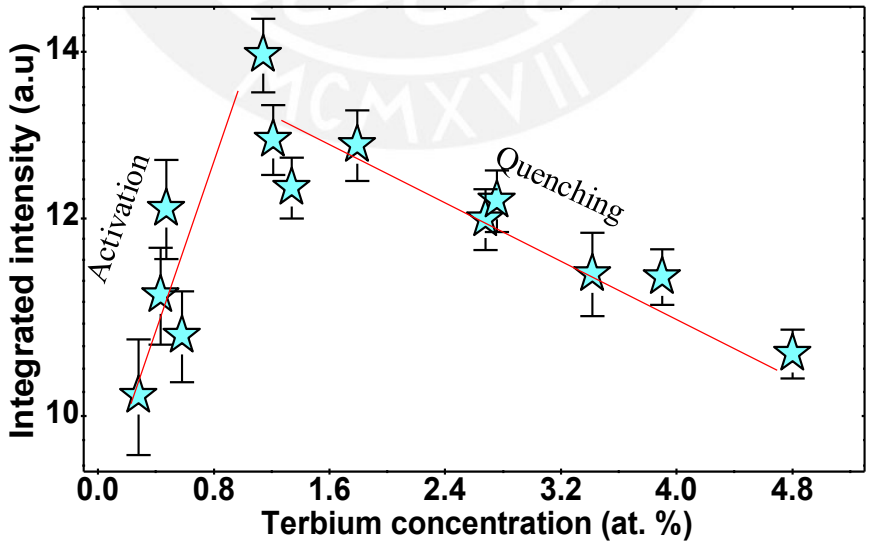

Figure 5.18 Integrated intensity of the $^5D_4 \rightarrow ^7F_5$ transition for the a- AlO_xN_y:Tb layers. Samples have terbium concentration in the range from 0.4 up to 4.8 at.%.

Figure 5.19 (a) shows the light intensity of the $^5D_4 \rightarrow {}^7F_5$ transition of the *a*- AlO_xN_y:Tb versus the annealing temperature of two set of samples: with and without etching. Samples without etching are represented by the yellow circles and the etched samples by the green circles. The light intensity of the $^5D_4 \rightarrow {}^7F_5$ transition increases until around 400 °C and afterward the emission decreases. Figure 5.19 (b) shows the area of the Tb_2O_3 versus the annealing treatment. Tb_2O_3 decreases with the annealing temperature until 750 C. At 1000 C the decrease of Tb_2O_3 is strong, however, it is compensated with the Tb_2O_3 from the O1s core level at 529.4 eV.

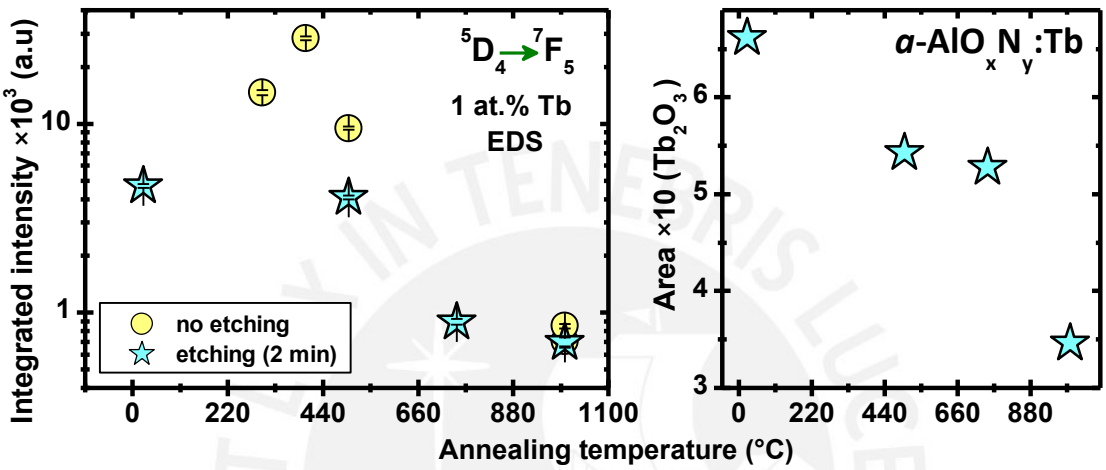

Figure 5.19 intensity (a) of the $^5D_4 \rightarrow {}^7F_5$ transition and Tb_2O_3 concentration in at. % (b) for the a-AlO_xN_y:Tb layers. According to the EDS, all the samples before the annealing temperature had a terbium concentration of around 1 at%.

EDX reveals a nearly constant composition of Tb after the annealing temperature. However, the concentration of Tb retrieved from the XPS core levels decreases with the annealing temperature. It could be happen due the diffusion of Tb through the cracks. Thus, the O-Tb bindings are decreasing, inducing the decrease in intensity of the 5D4→7F5 transition. Thus, the O-Tb bindings are decreasing, inducing the decrease in intensity of the $^5D_4 \rightarrow {}^7F_5$ transition.

Figure 5.20 shows the CL spectra for the *a*- SiC_xO_y:Tb at room temperature, and after annealing temperatures at 750 C and 1000 C. All the CL spectra exhibit only a strong emission of light correspondent to the host matrix, whereas no the characteristic $^5D_4 \rightarrow {}^7F_j$ transitions of the terbium. The insert RHEED diffuse patterns implies that the sample is amorphous, which is in good correlation with the XRD results. RHEED patterns for the *a*- SiC_xO_y:Tb heated at 1000 °C are also characteristic of amorphous materials.

In the case of the sample heated at 750 °C (Figure 5.20 b, c), diffuse and also well defining weak Bragg's spots patterns are observed. However, no crystalline phases were found in the XRD

patterns. Therefore, as in the case of the a- AlO_xN_y:Tb layers, the *a*- SiC_xO_y:Tb layers are amorphous, but with few crystalline regions.

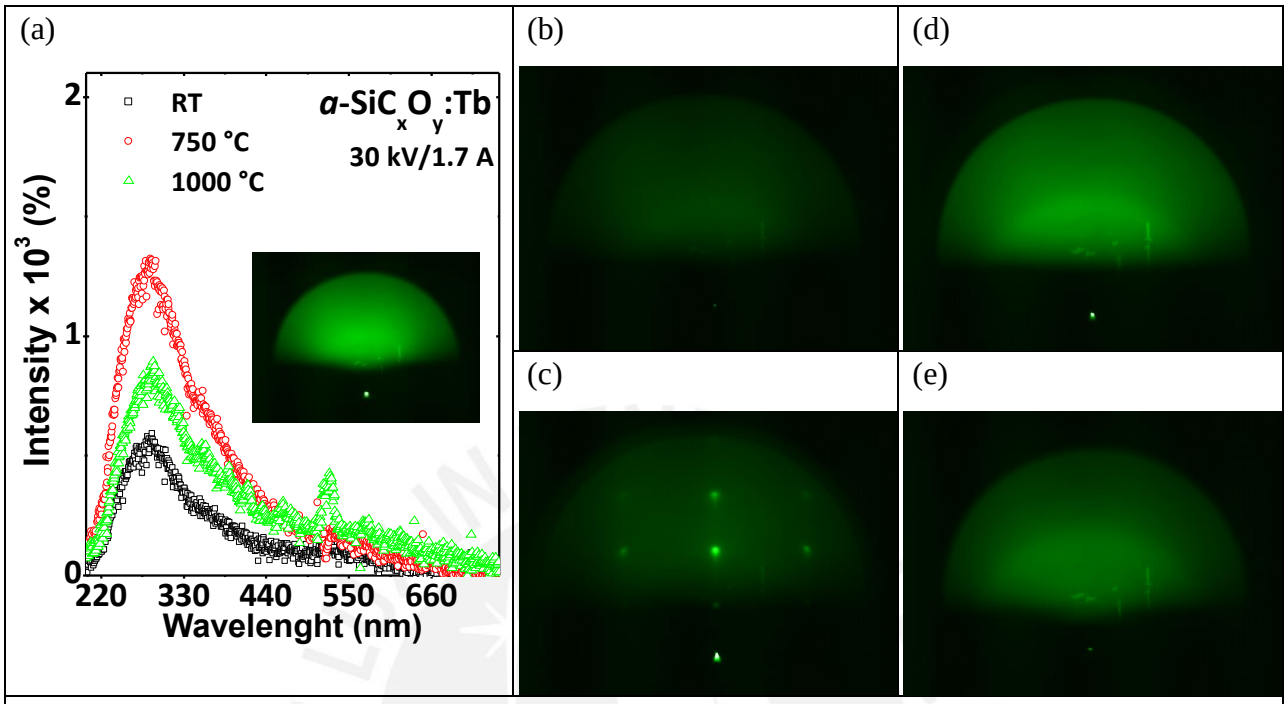

Figure 5.20 CL measurements for the a- SiC_xO_y:Tb layer at room temperature and after annealing temperatures at 750 °C and 1000 °C. The RHEED image is also included (a). RHEED images for the samples annealed at 750 °C (b-c) and at 1000 °C (d-e).

5.5.3. I-V curve. PL and EL analysis on the devices

Figure 5.21 shows the I-V curves for the ACTFEL and DCTFEL devices and the insert graphics show their respective PL spectra. The structure of the ACTFEL device is composed of *a*- AlO_xN_y:Tb (600 nm) as the active material and Mo (150 nm) and ITO (150 nm) as metal and transparent electrodes and Si_3N_4 (100 nm) as the insulating layer. Figure 5.21 (a) shows the I-V curve of the ACTFEL device. The V_{th} around 170 V was found, which means that current is flowing through the active layer, and therefore, light emission should be expected. However, no light emission is observed when current is applied through the devices.

The structure of the DCTFEL device is composed of ZnO (15 nm) as ETL layer and WO_3 (10 nm) and WC (10 nm) as HTL layers. The I-V curve for the DCTFEL devices was retrieved by applying low voltages of around 5 eV through the electrodes of the devices. The idea was increasing the voltage in steps of 1 eV until the threshold voltage (V_{th}) is reached. Nevertheless, no V_{th} is observed instead, an Ohmic behavior was obtained. Ohmic behavior can be obtained due short-circuit between the Mo/ITO electrodes.

The problems of no emission of the devices could be in the manufacturing of the device, electrodes or in the active layer. The active layer is amorphous and thus, it can have defect states in the bandgap. Non-radiative transition and cross-relaxation can take advantages of the defect states and, therefore, they can extinguish emission of light.

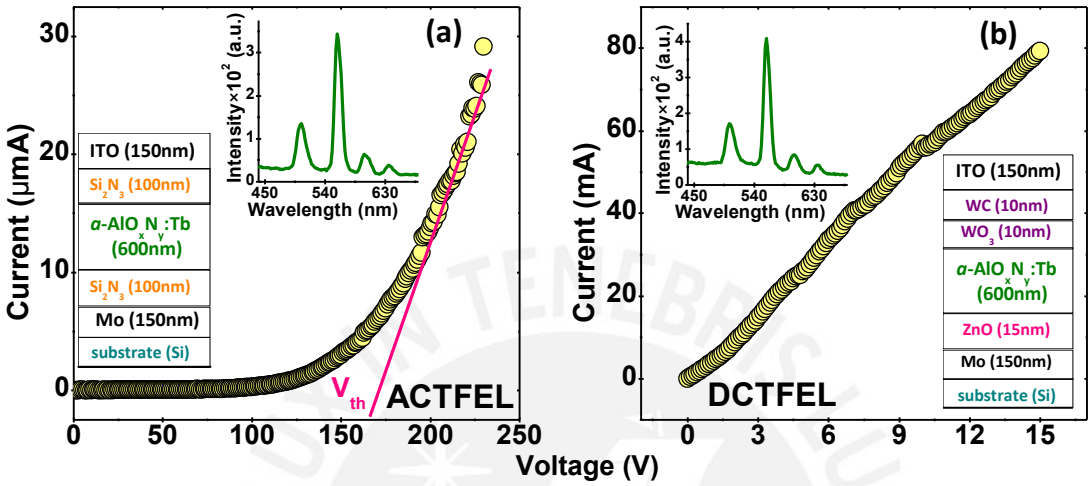

Figure 5.21 I-V curve measurements of the ACTFEL (a) and DCTFEL (b) devices structure. Each graphic includes the PL measurement of the device and also the device structure.

a) Challenges in the production of the DCTFEL and ACTFEL devices

Conventional and inverted ACTFEL and DCTFEL were planned to be designed. The effect of the thickness of different insulator layer was wanted to be studied for the case of the ACTFEL devices. Different HTL/ETL layers were planned to be incorporated in the design of the DCTFEL devices. However, the devices were peeled during the deposition of the active layer. One of the challenges in the deposition of the active layers was that the cooling system failed and, therefore, the plasma maintained the samples hot during the deposition process producing a poor adherence between the substrate and the layer. Another problem is the non-uniformity cooling of the substrate holder. The challenges in the manufacturing of the devices are the following.

1. HTL and ETL were included in the structure of the DCTFEL devices in order improve the injection of holes and electrons. The decision of the HTL/ETL layers were for *a*-AlN:Tb and *a*- SiC:Tb layers. However, no suitable *a*- AlO_xN_y:Tb and *a*- SiC_xO_y:Tb layers were obtained. Therefore, no injection of electrons and holes was possible due the differences in the work functions of the HTL/ETL layers and the band offsets of the *a*-AlO_xN_y:Tb.

2. *a*-SiC_xO_y:Tb layer do not show the characteristic $^5D_4 \rightarrow ^7F_j$ transition, only the host matrix emission is observed (Figure 5.20 a). After the annealing temperature, there is also no emission of light of terbium.

3. Inverted ACTFEL devices were designed in order to use molybdenum as the electrode and, therefore, heated the device at high temperatures (around 750 °C) in order to activate the Terbium. However, after the annealing, the samples presented fracture appearance (see Figure 5.1).

b) Suggestions for further design of DCTFEL and ACTFEL devices.

1. There are two ways to improve the first challenge. First, produce as active layer crystalline AlN:Tb layers in order to use the proposed HTLs and ETL. Second, chose other HTL/ETL, which better match the difference between the work function of the electrodes and the band offsets of the *a*- AlO_xN_y:Tb.

2. For the second challenge, better deposition parameters for the grown of the *a*-SiC_xO_y:Tb should be found in order to have the characteristic $^5D_4 \rightarrow ^7F_j$ transition. According to the literature, it has been demonstrated that SiCN is a good host matrix for the terbium [75]. Therefore, one possible change in the deposition of the samples could be the use of nitrogen instead hydrogen.

6. Future works

- Since the design of the ACTFEL and DCTFEL was performed taking as reference the AlN:Tb and SiC:Tb as active layers, the first step to improve the El devices will be the reduction of oxygen in this layers.

- The election of HTL and ETL is a challenge since the knowing of the band offsets of the active layer is necessary in order to make a good matching of the work functions and band offsets. An alternative for this challenge is the use of an active layer with different bandgaps.

  Figure 6.1 (a) shows the variation of the bandgap of the *a*-$(SiC)_{1-x}(AlN)_x$ compound as a function of the composition (bandgap engineering). Figure 6.1 (b) shows the structure of the TCO electrode, which has small areas in order to measure EL in different areas. Since this active layer has different bandgaps, one region will be suitable to the HTL and ETL

(a) (b)

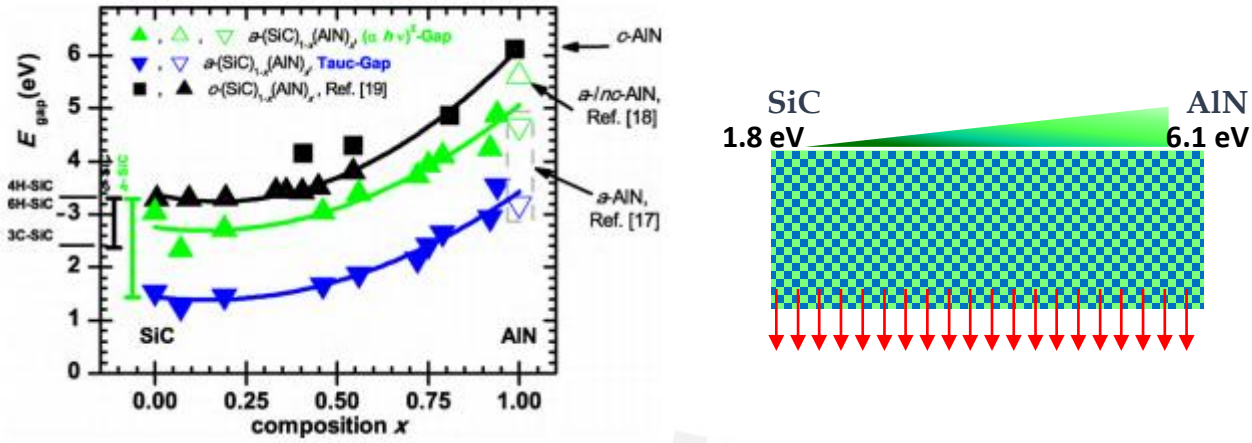

Figure 6.1 I-V Bandgap engineering of the a-SiC and a-AlN layers [76] ***(a) and TCO structure electrodes proposed for the DCTFEL (b) device.***

7. Conclusions

Active layers were grown by a radiofrequency magnetron sputtering using flexible targets of SiC (with nitrogen as the main impurity and less than 10 ppm), AlN (with oxygen impurity below 90 ppm) and Tb (3N purity). In the present work, stoichiometric, structural and light emission properties of those amorphous wide bandgap semiconductor materials doped with terbium have been investigated. The characterized materials were also incorporated in the manufacture of the EL devices. From this research work the following are concluded.

1. Characterization of the active layers

- Because of the flexible geometry of the magnetron different Tb concentration are found in one process, therefore, several EDX measurements were carried out every 2.5 mm in two samples of dimensions around 40 mm×15 mm. Terbium concentration can be decrease or oscillate. It depends on the position of the samples in the substrate holder. (Figure 5.5). The advantage of the flexible geometry of the magnetrons is the possibility to reach different Tb concentration in one process.

- XRD patterns of the AlO_xN_y:Tb active layers in the as deposited state (Figure 5.6). reveal an amorphous state with partial crystalline areas. Thus, amorphous samples were chosen and heated at temperatures of 500 °C, 750 °C and 1000 °C. The sample remains amorphous at 500 °C and 750 °C. In contrast, at 1000 °C the sample presents a cubic crystalline structure corresponding to the Al_5O_6N. Its crystallographic orientations assigned to the (400) and (440) have grain sizes of 10.4 nm and 11.2 nm, respectively. However, the peaks in the XRD pattern are shifted compared to the theoretical positions shown in the literature. This fact could be due residual stress.

- XRD patterns confirm the amorphous nature of the *a*- SiC_xO_y:Tb layer before and after the annealing temperatures. Nevertheless, RHEED images in different positions of the sample heated at 750 °C present diffuse and also well defining weak Bragg's spots patterns (Figure 5.20). Therefore, is possible to conclude that the *a*- SiC_xO_y:Tb presents an amorphous state with partial crystalline areas.

- SEM images show a cluster like morphology in the as-deposited state for all the samples. The cluster is more evident for the un-doped AlO_xN_y layer, even when the XRD pattern shows an amorphous state. However, XRD result is an average of the whole area of the samples, whereas the SEM provides images only of a small area.

- After annealing temperature in an RTP furnace, the surface morphology of the *a*- SiC_xO_y:Tb presents tiny grains. In contrast, the surface morphology of the *a*- AlO_xN_y:Tb layers present tiny grains and fracture appearance. Cracking formation after the heating

could be due the difference in thermal expansion coefficient between the substrate and film and residual stress.

- Al-N, Al-O, Al-O-Al and O-H vibrational modes were found for samples grown using AlN and Tb target, whereas Si-C, Si-O-Si and Si-O for samples grown using SiC and Tb targets. The dominant vibrational modes are the Al-O and the Si-O. These results suggest the formation of *a*- AlO_xN_y:Tb and *a*- SiC_xO_y:Tb and this fact was confirmed by the XPS measurement. In contrast to the *a*- SiC_xO_y:Tb, the *a*- AlO_xN_y:Tb present a high O-H vibrational mode at room temperature and it disappears with the annealing temperature. This fact, suggest the incorporation of humidity in the films. Cracking formation observed in the SEM images after the heating processes could be due the degassing of the H-O vibrational modes.

- Tb3d core level shows the direct bonds of the terbium with the oxygen. The area of the Tb_2O_3 at binding energies of 1240 °eV decreases with the annealing temperature. At 1000 °C the decrease of the Tb_2O_3 at 1240 °eV is strong, but there is also the formation of in the Tb_2O_3 O1s core level.

- PL results of the *a*- AlO_xN_y:Tb film with different terbium concentration shows two visible regions. In the first region, light emission of terbium is enhanced with the increasing of Terbium atoms (Activation). In the second region, the incorporation of more terbium atoms produces extinction of light emission (quenching). Concentration quenching could happen due the clustering of the Terbium ions.

- The annealing temperature enhances the emission of light of terbium until around 400 °C, after that, the emission of light from the PL spectra decreases. CL spectrum, in accordance with the PL also presents a decreases in light intensity. The decreasing of light emission could be related to the decreasing in the area of the Tb_2O_3 from the Tb3d core levels (Figure 5.19).

- Regarding the characterization part, the best parameters for the production of the EL devices should be samples with terbium concentration in the range of 1 to 2 at% and at room temperature in order to avoid fracturing in the active layer.

2. Design and fabrication of the EL devices

Two kinds of conventional and inverted EL devices were planned to be designed. The structure of the DCTFEL device includes HTL and ETL layers, whereas the structure of ACTFEL device includes insulating layers. PL on the EL devices exhibits the characteristic $^5D_4 \rightarrow {}^7F_j$ transitions, however, when the current was applied to the devices no light emission was observed.

- In the case of the DCTFEL device, the unsuitable grown of the *a*- AlO_xN_y:Tb instead AlN:Tb will affect the performance of the device, since the selection of the HTL and ETL are chosen in reference to the band offsets of the active layer. However, the knowledge of the work functions of the active layers, electrodes and HTL and ETL is a critical point for the performance of the devices. Information of the band offsets of the active layer is also necessary. The proposed scheme for the EL devices (Figure 6.1) is viable since it not requires an exact value of the work functions.

- ACTFEL do not depend on the work function of the electrodes, since the injection of charges is directly from the interfaces insulator/active layer. Therefore, the growth of *a*- AlO_xN_y:Tb instead AlN:Tb as active layer will not affect the manufacturing of the AC devices, but the quality of the layer can extinguish the emission of light. I-V curve of these devices shows clearly a threshold voltage of 170 V, it means that, there is injection of charges into the active layer. However, non-radiative processes and cross-relaxation overcome the radiative process. Nonetheless, another problem in the manufacturing of the devices could be the unwanted heating of the samples during the deposition of the insulating layer and, therefore, the fracturing of the active layer.

Acknowledgments

I want to express my gratitude and thanks to all the people who supported me during the development of this thesis and also to the funding sources which make possible to accomplish and end this research work.

I would like to thank to my supervisors Dr. Roland Weingärtner and Dr. Harald Hoppe who advised and supported me during my Master time. Many thanks to Prof. Dr. rer. nat. habil. Peter Schaaf for giving me the opportunity to use the equipments in the clean room at the IMN in Ilmenau. Thanks to Dr. Rolf Grieseler who taught me how to manage the SEM, XRD and sputtering equipments, for responded my queries and helped me to find all the things that I need for this thesis promptly and also for his patience and suggestions for the development of this thesis content.

I want to thank many members of the PUCP and TU-Ilmenau. To Prof. Dr. Stefan Krischok and Dr. Marcel Himmerlich for allowing me the performance of the XPS measurements and to M.Sc. Stephanie Reiß who did the XPS measures and also for teaching me the analysis of these data. To Dr. rer. nat. Jörg Pezoldt who did the CL and RHEED measures and also to allow me to do the FTIR measures. I am sincerely grateful to Dipl.-Phys. Peter Fischer who helped and taught me how structured the electrodes of the devices and for his kindness and support during my studies. Especial thanks to Alvaro Tejada Esteves for his time and patience in depositing of the active materials for the devices and also for his friendship.

I would like to express my gratitude to Prof. Wolfgang Skorupa and Dr. Lars Rebohle for giving me the opportunity to visit their Labs. at Helmholtz Zentrum Dresden Rossendorf (HZDR) for the performance of the PL, EL and C-V measurements and to Dr. Yonder Berencen who taught me those techniques.

Finally, but not least I want to thank to all the Professors for the interesting lectures, to my colleagues in the classroom and in the laboratory and to the family Fischer for the nice moments during my internship.

This master thesis was financed by the FONDECYT (PUCP-FONDECYT 012-2013) of Perú and supported by the research office (DGI) of the Pontificia Universidad Católica del Perú and for the “Círculos de Investigación en Ciencia y Tecnología” program of the CONCYTEC of Perú.

8. References

[1] O. Madelung, Semiconductors: Data Handbook, 3ra editio, Springer, Germany, 2004. doi:978-3-642-18865-7.

[2] B.N. Pantha, R. Dahal, M.L. Nakarmi, N. Nepal, J. Li, J.Y. Lin, et al., Correlation between optoelectronic and structural properties and epilayer thickness of AlN, Appl. Phys. Lett. 90 (2007) 3–5. doi:10.1063/1.2747662.

[3] K.H. Kim, Z.Y. Fan, M. Khizar, M.L. Nakarmi, J.Y. Lin, H.X. Jiang, AlGaN-based ultraviolet light-emitting diodes grown on AlN epilayers, Appl. Phys. Lett. 85 (2004) 4777. doi:10.1063/1.1819506.

[4] P.M. Kaminski, K. Bass, G. Claudio, High bandgap dielectrics for antireflective coating in silicon solar cells by reactive ion sputtering, Phys. Status Solidi Curr. Top. Solid State Phys. 8 (2011) 1311–1314. doi:10.1002/pssc.201084008.

[5] G. Krugel, F. Jenkner, A. Moldovan, W. Wolke, J. Rentsch, R. Preu, Investigations on the Passivation Mechanism of AlN:H and AlN:H-SiN:H Stacks, Energy Procedia. 55 (2014) 797–804. doi:10.1016/j.egypro.2014.08.062.

[6] F. Liu, C. Carraro, A.P. Pisano, R. Maboudian, Growth and characterization of nitrogen-doped polycrystalline 3C-SiC thin films for harsh environment MEMS applications, J. Micromechanics Microengineering. 20 (2010) 035011. doi:10.1088/0960-1317/20/3/035011.

[7] M.A. Fraga, M. Massi, I.C. Oliveira, H.S. Maciel, S.G. dos Santos Filho, R.D. Mansano, Nitrogen doping of SiC thin films deposited by RF magnetron sputtering, J. Mater. Sci. Mater. Electron. 19 (2007) 835–840. doi:10.1007/s10854-007-9487-y.

[8] F. Alibarta, O. Durand Drouhina, C. Debiemme-Chouvyb, M. Benlahsen, Relationship between the structure and the optical and electrical properties of reactively sputtered carbon nitride films, Solid State Commun. 147 (2008) 392–396. doi:doi:10.1016/j.ssc.2007.11.025.

[9] F. Zhu, J. Hu, I. Matulionis, T. Deutsch, N. Gaillard, a. Kunrath, et al., Amorphous silicon carbide photoelectrode for hydrogen production directly from water using sunlight, Philos. Mag. 89 (2009) 2723–2739. doi:10.1080/14786430902740729.

[10] J. a Guerra, L. Montañez, O. Erlenbach, G. Galvez, F. De Zela, a Winnacker, et al., Determination of the optical bandgap and disorder energies of thin amorphous SiC and AlN films produced by radio frequency magnetron sputtering, J. Phys. Conf. Ser. 274 (2011) 012113. doi:10.1088/1742-6596/274/1/012113.

[11] D. Adachi, Æ.R. Kitaike, Æ.J. Ota, Green electroluminescence from AlN : Tb thin film devices on glass, J. Mater. (2007) 71–74. doi:10.1007/s10854-007-9167-y.

[12] A.R. Zanatta, Photoluminescence quenching in Er-doped compounds, Appl. Phys. Lett. 82 (2003) 1395–1397. doi:10.1063/1.1557318.

[13] J.A. Guerra, F. Benz, A.R. Zanatta, H.P. Strunk, A. Winnacker, R. Weingärtner, Concentration quenching and thermal activation of the luminescence from terbium-doped a -SiC:H and c -AlN thin films, Phys. Status Solidi. 10 (2013) 68–71. doi:10.1002/pssc.201200394.

[14] H.J. Lozykowski, W.M. Jadwisienczak, I. Brown, Photoluminescence and cathodoluminescence of GaN doped with Pr, J. Appl. Phys. 88 (2000) 210–222. doi:10.1063/1.373645.

[15] A. Janotta, M. Schmidt, R. Janssen, M. Stutzmann, C. Buchal, Photoluminescence of Er+3 implanted amorphous hydrogenated silicon suboxides, Phys. Rev. B. 68 (2003) 165207. doi:10.1103/PhysRevB.68.165207.

[16] J. Heikenfeld, a. J. Steckl, Alternating current thin-film electroluminescence of GaN:Er, Appl. Phys. Lett. 77 (2000) 3520. doi:10.1063/1.1330564.

[17] H.H. Richardson, P.G. Van Patten, D.R. Richardson, M.E. Kordesch, Thin-film electroluminescent devices grown on plastic substrates using an amorphous AlN:Tb[sup 3+] phosphor, Appl. Phys. Lett. 80 (2002) 2207. doi:10.1063/1.1464220.

[18] H. Lian, Z. Hou, M. Shang, D. Geng, Y. Zhang, J. Lin, Rare earth ions doped phosphors for improving efficiencies of solar cells, Energy. 57 (2013) 270–283. doi:10.1016/j.energy.2013.05.019.

[19] K. Takahashi, A. Yoshikawa, A. Sandhu, eds., Wide bandgap semiconductors, Springer, 2007. doi:9783540472353.

[20] S. Montanari, Fabrication and characterization of planar Gunn diodes for Monolithic Microwave Integrated Circuits, 2004.

[21] S. Kasap, P. Capper, Springer Handbook of Electronic and Photonic Materials, 2006. doi:10.1007/978-0-387-29185-7.

[22] G.R. Fisher, P. Barnes, Towards a unified view of polytypism in silicon carbide, Philos. Mag. Part B. 61 (1990) 217–236. doi:10.1080/13642819008205522.

[23] M. Wijesundara, R. Azevedo, Silicon carbide microsystems for harsh environments, Springer, London, 2011. doi:10.1007/978-1-4419-7121-0.

[24] J.B. Casady, W. Johnson, Status of silicon carbide (SiC) as a wide bandgap semiconductor for high-temperature applications: a review, 39 (1996) 1409–1422.

[25] I. Yonenaga, Thermo-mechanical stability of wide-bandgap semiconductors: high temperature hardness of SiC, AlN, GaN, ZnO and ZnSe, Phys. B Condens. Matter. 308–310 (2001).

[26] Y.S. Park, SiC materials and devices, ACADEMIC PRESS, United States, 1998.

[27] H. Onuma, http://www.aki.che.tohoku.ac.jp/prev/htm6/2007_0226_ACCMS-VO-oonuma.files/frame.htm, (2007) 40. http://www.aki.che.tohoku.ac.jp/prev/htm6/2007_0226_ACCMS-VO-oonuma.files/frame.htm.

[28] R.-J. Xie, Y. Li, N. Hirosaki, H. Yamamoto, Nitride phosphors and solid-state lighting, Taylor & Francis, 2011.

[29] C. Huang, Rare earth coordination chemistry, 1997.

[30] J. Zmojda, M. Kochanowicz, P. Miluski, D. Dorosz, Side-Detecting Optical Fiber Doped with Tb3+ for Ultraviolet Sensor Application, Fibers. 2 (2014) 150–157. doi:10.3390/fib2020150.

[31] J.A. Guerra, L. Montañez, A. Winnacker, F. De Zela, R. Weingärtner, Thermal activation and temperature dependent PL and CL of Tb doped amorphous AlN and SiN thin films, Phys. Status Solidi. 4 (2015) n/a–n/a. doi:10.1002/pssc.201400226.

[32] S. Rein, Lifetime spectroscopy, Springer-Verlag Berlin Heidelberg, 2005.

[33] F. Auzel, Upconversion and anti-stokes processes with f and d ions in solids, Chem. Rev. 104 (2004) 139–173. doi:10.1021/cr020357g.

[34] Förster, Zwischenmolekulare Energiewanderung und Fluoreszenz, Ann. Der Phys. (1948).

[35] D.L. Dexter, A Theory of Sensitized Luminescence in Solids, J. Chem. Phys. 21 (1953) 836. doi:10.1063/1.1699044.

[36] H.K. Henisch, Electroluminescence, Pergamon Press, New York, 1962. doi:10.1346/CCMN.1967.0150147.

[37] K.F. Brennan, The physics of semiconductors, Cambridge University Press, 1999. doi:10.1049/ep.1967.0135.

[38] G. Mueller, ed., Electroluminescence II, ACADEMIC PRESS, 2000. doi:10.1017/CBO9781107415324.004.

[39] C. Singh, Solar photovoltaics: fundamentals, technologies and applications, PHI learning private limited, 2015.

[40] B. Thestrup, J. Schou, Transparent conducting AZO and ITO films produced by pulsed laser ablation at 355 nm, Appl. Phys. A Mater. Sci. Process. 69 (1999) S807–S810. doi:10.1007/s003390051535.

[41] V.I. Dimitrova, P.G. Van Patten, H.H. Richardson, M.E. Kordesch, Visible emission from electroluminescent devices using an amorphous AlN:ErTb3+ thin film phosphor, Appl. Phys. Lett. 77 (2000) 478. doi:10.1063/1.127016.

[42] P.O. Anikeeva, C.F. Madigan, J.E. Halpert, M.G. Bawendi, V. Bulović, Electronic and excitonic processes in light-emitting devices based on organic materials and colloidal

quantum dots, Phys. Rev. B. 78 (2008) 085434. doi:10.1103/PhysRevB.78.085434.

[43] J. Holzl, F.K. Schulte, Work function of metals, Solid Surf. Phys. (1979).

[44] Y.J. Lin, F.M. Yang, C.Y. Huang, W.Y. Chou, J. Chang, Y.C. Lien, Increasing the work function of poly(3,4-ethylenedioxythiophene) doped with poly(4-styrenesulfonate) by ultraviolet irradiation, Appl. Phys. Lett. 91 (2007) 2007–2009. doi:10.1063/1.2777147.

[45] H.W. Hugosson, O. Eriksson, U. Jansson, A. V. Ruban, P. Souvatzis, I.A. Abrikosov, Surface energies and work functions of the transition metal carbides, Surf. Sci. 557 (2004) 243–254. doi:10.1016/j.susc.2004.03.050.

[46] T.-L. Chiu, Y.-T. Chuang, Spectral observations of hole injection with transition metal oxides for an efficient organic light-emitting diode, J. Phys. D. Appl. Phys. 48 (2015) 075101. doi:10.1088/0022-3727/48/7/075101.

[47] C. Tao, S. Ruan, G. Xie, X. Kong, L. Shen, F. Meng, et al., Role of tungsten oxide in inverted polymer solar cells, Appl. Phys. Lett. 94 (2009) 2–4. doi:10.1063/1.3076134.

[48] S. Gutmann, M. Conrad, M.A. Wolak, M.M. Beerbom, R. Schlaf, Work function measurements on nano-crystalline zinc oxide surfaces, J. Appl. Phys. 111 (2012). doi:10.1063/1.4729527.

[49] Y. Ono, Electroluminescent displays, World Scientific Publishing Company, USA, 1995.

[50] R. Brundle, C. Evans, C. Wilson, Encyclopedia of material characterization, Butterwornth-Heineman, 1992.

[51] R.A. Street, Hydrogenated amorphous silicon, Cambridge University Press, NewYyork, 1991.

[52] k. Wassa, S. Hayakawa, Handbook of sputter deposition technology, Mill Road, Park Ridge, New Jersey 07656, United Satates, 1992.

[53] A.H. Simon, 4 Sputter Processing, 2012.

[54] M.M. Waite, W. Chester, D. a Glocker, I. Incorporated, N. York, Sputtering Sources, SVC Bull. Spring. (2010) 42–50.

[55] W. Zhou, Z. Wang, Scanning Microscopy for Nanotechnology: Techniques and Applications, Springer, 2006.

[56] D. Brandon, W. Kaplan, Microstructural characterization of materials, John Wiley & Sons Ltd, England, 1999.

[57] J. Goldstein, D. Newbury, D. Joy, C. Lyman, P. Echlin, E. Lifshin, et al., Scanning and transmission electron microscopy and X-ray microanalysis, n.d.

[58] S. Flegler, J. Heckman, K. Klomparens, Scanning and transmission electron microscopy, W. H. Freeman and company, New York, 19993.

[59] J. Wachtman, Characterization of materials, United States, 1993.

[60] Y. Leng, Materials characterization: Introduction to Microscopic and Spectroscopic Methods, 2008.

[61] P. Scherrer, Bestimmung der Größe und der inneren Struktur von Kolloidteilchen mittels Röntgenstrahlen, (1918). http://resolver.sub.uni-goettingen.de/purl?PPN252457811_1918/dmdlog15.

[62] B. Stuart, Infrared spectroscopy: fundamentals and application, 2013. doi:10.1017/CBO9781107415324.004.

[63] Q. WEI, X. ZHANG, D. LIU, J. LI, K. ZHOU, D. ZHANG, et al., Effects of sputtering pressure on nanostructure and nanomechanical properties of AlN films prepared by RF reactive sputtering, Trans. Nonferrous Met. Soc. China. 24 (2014) 2845–2855. doi:10.1016/S1003-6326(14)63417-8.

[64] L. Yang, Y. Tang, A. Hu, X. Chen, K. Liang, L. Zhang, Raman scattering and luminescence study on arrays of ZnO doped with Tb3+, Phys. B Condens. Matter. 403 (2008) 2230–2234. doi:10.1016/j.physb.2007.12.013.

[65] J.F. Moulder, W.F. Stickle, P.E. Sobol, K.D. Bomben, Handbool of X-ray Photoelectron Spectroscopy, (1995) 255.

[66] M. Kazan, B. Rufflé, C. Zgheib, P. Masri, Oxygen behavior in aluminum nitride, J. Appl. Phys. 98 (2005) 103529. doi:10.1063/1.2137461.

[67] H. Cheng, Y. Sun, J.X. Zhang, Y.B. Zhang, S. Yuan, P. Hing, AlN films deposited under various nitrogen concentrations by RF reactive sputtering, J. Cryst. Growth. 254 (2003) 46–54. doi:10.1016/S0022-0248(03)01176-X.

[68] J. Ning, S. Xu, K.N. Ostrikov, J.W. Chai, Y.N. Li, K.M. Ling, et al., Synthesis and structural properties of Al-C-N-O composite thin films, Thin Solid Films. 385 (2001) 55–60. doi:Doi 10.1016/S0040-6090(00)01923-4.

[69] V. Vamvakas, D. Davazoglou, Comparison of FTIR Transmission Spectra of Thermally and LPCVD SiO2 Films Grown by TEOS Pyrolysis, J. Electrochem. Soc. 151 (2004) F93–F97. doi:10.1149/1.1676725.

[70] S. Gallis, M. Huang, H. Efstathiadis, E. Eisenbraun, A.E. Kaloyeros, E.E. Nyein, et al., Photoluminescence in erbium doped amorphous silicon oxycarbide thin films, Appl. Phys. Lett. 87 (2005) 99–101. doi:10.1063/1.2032600.

[71] S. Gallis, V. Nikas, H. Suhag, M. Huang, A.E. Kaloyeros, White light emission from amorphous silicon oxycarbide (a-SiCx Oy) thin films: Role of composition and postdeposition annealing, Appl. Phys. Lett. 97 (2010) 2008–2011. doi:10.1063/1.3482938.

[72] J. V. Ryan, C.G. Pantano, Synthesis and characterization of inorganic silicon oxycarbide glass thin films by reactive rf-magnetron sputtering, J. Vac. Sci. Technol. A Vacuum, Surfaces, Film. 25 (2007) 153. doi:10.1116/1.2404688.

[73] L.M. Montañez, J.A. Guerra, K. Zegarra, S. Kreppel, F. De Zela, A. Winnacker, et al., Optical bandgap enhancement of a -SiC through hydrogen incorporation and thermal annealing treatments, Proc. SPIE - Int. Soc. Opt. Eng. 8785 (2013) 87859S. doi:10.1117/12.2027656.

[74] V. Kumar, S. Som, V. Kumar, V. Kumar, O.M. Ntwaeaborwa, E. Coetsee, et al., Tunable and white emission from ZnO : Tb 3 + nanophosphors for solid state lighting applications, Chem. Eng. J. 255 (2014) 541–552. doi:10.1016/j.cej.2014.06.027.

[75] Z. Chen, J. Zhou, X. Song, X. Xu, Y. Liu, J. Song, et al., The effect of annealing temperatures on morphologies and photoluminescence properties of terbium-doped SiCN films, Opt. Mater. (Amst). 32 (2010) 1077–1084. doi:10.1016/j.optmat.2010.03.001.

[76] R. Weingärtner, J.A. Guerra, O. Erlenbach, F. Gálvez, F. De Zela, A. Winnacker, Bandgap engineering of the amorphous wide bandgap semiconductor (SiC)1−x(AlN)x doped with terbium and its optical emission properties, Mater. Sci. Eng. 174 (2010) 114–118.